Chinese Journal of Chemical Engineering 32 (2021) 39–60

Contents lists available at ScienceDirect

Chinese Journal of Chemical Engineering

journal homepage: www.elsevier.com/locate/CJChE

Article

Experimental and Numerical Study of Gas-Liquid Flow in a Sectionalized External-Loop Airlift Reactor

Shivanand M. Teli [1,2,*], Channamallikarjun S. Mathpati [1]

[1] Department of Chemical Engineering, Institute of Chemical Technology, Mumbai, India
[2] Department of Chemical Engineering, Gharda Institute of Technology, Khed, Ratnagiri, India

ARTICLE INFO

Article history:
Received 14 February 2020
Received in revised form 18 September 2020
Accepted 2 October 2020
Available online 27 November 2020

Keywords:
Multiphase reactor
Bioreactors
Computational fluid dynamic
Sectionalised external loop airlift reactor
Gas hold up
Mass transfer

ABSTRACT

The external loop airlift reactor (EL-ALR) is widely used for gas-liquid reactions. It's advantage of good heat and mass transfer rates compared to conventional bubble column reactors. In the case of fermentation application where a medium is highly viscous and coalescing in nature, internal in riser helps in the improvement of the interfacial area as well as in the reduction of liquid- phase back mixing. The computational fluid dynamic (CFD) as a tool is used to design and scale-up of sectionalized external loop airlift reactor. The present work deals with computational fluid dynamics (CFD) techniques and experimental measurement of a gas hold-up, liquid circulation velocity, liquid axial velocity, Sauter mean bubble diameter over a broad range of superficial gas velocity $0.0024 \leq U_G \leq 0.0168$ m·s^{-1}. The correlation has been made for bubble size distribution with specific power consumption for different plate configurations. The effects of an internal on different mass transfer models have been completed to assess their suitability. The predicted local mass transfer coefficient has been found higher in the sectionalized external loop airlift reactor than the conventional EL-ALR.

© 2021 The Chemical Industry and Engineering Society of China, and Chemical Industry Press Co., Ltd. All rights reserved.

1. Introduction

Airlift reactors are currently gaining on increased interest in chemical engineering and biotechnology due to their number of advantages: producing efficient mass and heat transfer, high fluid circulation rate and low pressure drop. There is no moving part in the airlift reactor as results of it. This reactor offers another advantage *i.e*. low shear stress as compared to mechanically stirred tank reactors and bubble column reactor. The loop reactors are used in biochemical applications as level of shear stress is low, in them which allows micro–organisms to grow rather than to get broken down in presence of high shear stress. Gas hold-up and liquid circulation velocity are an important parameter for design, modelling, as well as for scale-up of airlift reactor. In this type of fermentation process, biochemical operation where the media is highly coalescing in nature, the bubble coalescence occurs. There are various parameters which one needs to control in ordered to avoid coalescence but gas velocity is the most prominent parameter that influence the coalescence process among bubble size, geometrical arrangement, temperature, phase properties density, viscosity, surface tension, Additives, *etc*. The mixing and mass transfer ability is highly depends upon the rheological properties of the broth. The viscous nature of fermentation broths is effect on many factors and process conditions inside the bioreactor. In this external airlift reactor with internal plates, each section within the reactor acts as a continuous stirred tank reactor (CSTR). CSTR is connected in series provide more conversion.

The fermentation broth having high coalescence media requires high mass transfer coefficient and interfacial area of the bubble. Due to internal plates in exteral loop airlift reactor (EL-ALR), it is possible to give a small bubble size distribution. As the size of bubble is small, the terminal rise velocity of the bubble becomes less. The terminal rise velocity of a bubble is directly proportional to the diameter of bubbles. It is difficult to predict the performance external loop airlift reactor due to complex geometries and hydrodynamic behaviour. The laboratory-scale airlift reactors with internal are not much investigated therefore. Computation fluid dynamic which is a tool of modelling used to investigate complex flow structure and type of mixing in the sectionalized external loop airlift reactor.

Many researchers [1–5] across the world have put their valuable time in understanding the hydrodynamic performance of air-

* Corresponding author at: Department of Chemical Engineering, Gharda Institute of Technology, Lavel, India. Fax: 02356 262980.
E-mail address: smteli@git-india.edu.in (S.M. Teli).

https://doi.org/10.1016/j.cjche.2020.10.023
1004-9541/© 2021 The Chemical Industry and Engineering Society of China, and Chemical Industry Press Co., Ltd. All rights reserved.

lift reactors. The hydrodynamic study of the external loop airlift reactor has been investigated [2,4] for the various ratios of the diameter of a riser to downcomer. The effect of hydrodynamic parameters due to different liquid level in the gas-liquid separator is also discussed in the literature. Various researchers [6–15] have developed the CFD model for the gas-liquid flow in the airlift reactors. Also, they have used different geometric and turbulent models to simulate the gas-liquid flow in the airlift reactor as shown in Table 1. The mixing time and residence time distribution study in sectionalized bubble column reactor has been reported in literature [16,17]. The hydrodynamic parameters are determined in multi-stage bubble column reactor in the literature [18,19]. Experimental study in the external loop airlift reactor with sieve plate and expansion disk have been discussed in the literature [20,21]. The hydrodynamic study in sectionalised external loop airlift reactor is already reported in literature [22].

In spite of so many published works, which describe the hydrodynamic studies, none of the CFD simulations have been done for sectionalized bubble column reactor and external loop airlift reactor.

In this present work, a CFD simulation of the sectionalized external loop airlift reactor has been performed. The k-epsilon turbulence model is used in this simulation. The effect of different plate configurations on gas hold-up, bubble size distribution, average liquid circulation velocity, and liquid axial velocity is determined. The proposed design will help to get a smaller bubble size distribution due sectionalisation.

Further, the CFD model has been extended for the prediction of the overall mass transfer coefficient. Different mass transfer models such as Penetration, eddy cell, rigid cell, and slip velocity model have been compared with different plate configurations.

The objectives of this study are observing the effect of internal on gas hold-up, liquid circulation velocity, liquid axial velocity, bubble size distribution, mass transfer coefficient in an external loop airlift reactor, comparison of different mass transfer model from CFD simulation for sectionalized external loop airlift reactor, and development of validated CFD model for scale-up and design of sectionalized external loop airlift reactor.

2. Experimental

The schematic of the EL-ALR is shown in Fig. 1. The lab-scale EL-ALR is made of acrylic transparent material. The geometrical dimension of a sectionalized external loop airlift reactor is as shown in given Table 2. The reactor has a perforated plate gas sparger with 17 circular holes with a 3 mm diameter. Tap water is used as a continuous fluid. Air is used as a dispersed phase sparged at the bottom of the column. All the experiments have been carried out at room temperature. The experiments have been carried out in a semi-batch mode *i.e.* initially air was supplied to the reactor continuously and water is already filled in the reactor. The gas hold-up and liquid circulation velocity are measured by a pressure transducer and conductivity probes connected at the bottom and top of the riser section. Table 3 provides the details of the experiments conducted.

2.1. Model parameter estimations

2.1.1. Gas hold-up (ε_G)

The pressure monitoring system, consisting of 2 pressure channels and a computer has been used to acquire the pressure data at a sampling frequency of 10 Hz. The range of the pressure is 0–30 psi (1 psi = 6.895 kPa). The pressure drop is measured by two pressure sensors placed in the riser at 1 m distance. Pressure Sensor has 0.1% accuracy and stainless steel (SS) body with 25%"

Table 1
Summary of previous work

Author (year)	Geometry/m	Superficial velocities/m·s^{-1}	Turbulence model	CFD code	Approach	Bubble diameter/mm	Drag force coefficient	Lift force coefficient	Turbulent dispersion	Virtual mass force coefficient
C. Lu (2009) [6]	D_r = 0.186 D_d = 0.042	U_G = 0.0059 to 0.1895	k-epsilon standard	ANSYS CFX 10	Euler -Euler	—	Grace	NA	NA	NA
N. Moudoud *et al.* (2018) [7]	D_r = 0.063 D_d = 0.107	U_G = 0.0253 to 0.0703	k-epsilon RNG	—	Euler -Euler	D_b = 3–4	Schiller and Numan	C_L = 0.5	NA	C_{vm} = 0.5
Z. Chen (2016) [8]	Width = 0.320 depth = 0.400	—	k-epsilon standard	ANSYS CFX 13	Euler -Euler	NA	Grace	NA	NA	NA
S.B. Pawar (2017) [9]	D_r = 0.010 D_c = 0.15	U_G = 0.01 to 0.06	k-epsilon standard	ANSYS CFX 10	Euler-Lagra	D_b = 1–15	Grace, Schiller and Numan, Ishii-Zuber	NA	NA	C_{vm} = 0.5
S. Roy *et al.* (2006) [10]	D_r = 0.2 D_d = 0.1	U_G = 0.0052 to 0.171	k-epsilon standard	ANSYS CFX 5.7.1	Euler -Euler	D_b = 2–6	Zhang and Vanderheyden	C_L = 0.5	CTD = 0.2	Negligible
S. Roy *et al.* (2008) [11]	D_r = 0.2 D_d = 0.1	U_G = 0.0096 to 0.084	k-epsilon standard	ANSYS CFX 10	Euler -Euler	D_b = 4–9	Zhang and Vanderheyden	C_L as per bubble size	CTD = 0.1	Negligible
K. M. Dhanasekharan *et al.* (2005) [12]	D_r = 0.07 D_d = 0.155	U_G = 0.01 to 0.05	k-epsilon standard	ANSYS FLUENT 6	Euler -Euler	—	Schiller and Numan	NA	NA	C_{vm} = 0.5
J. Karcz *et al.* (2013) [13]	D_r = 0.1056 D_d = 0.046	U_G = 0.013	k-epsilon standard	ANSYS CFX 13	Euler -Euler	D_b = 5	—	NA	NA	—
D. Law *et al.* (2009) [15]	D_r = 0.102 D_d = 0.025	U_G = 0.01 to 0.2	k-epsilon standard	CFDLib	Euler -Euler	D_b = 4 to 6	Schiller and Numan	NA	NA	C_{vm} = 0.5
Present work	D_r = 0.094 D_d = 0.047	U_G = 0.0024 to 0.012	k-epsilon standard							
	ANSYS FLUENT 14	Euler -Euler	D_b = 9.4–8.33	Grace	C_L as per bubble size	NA	C_{vm} = 0.5			

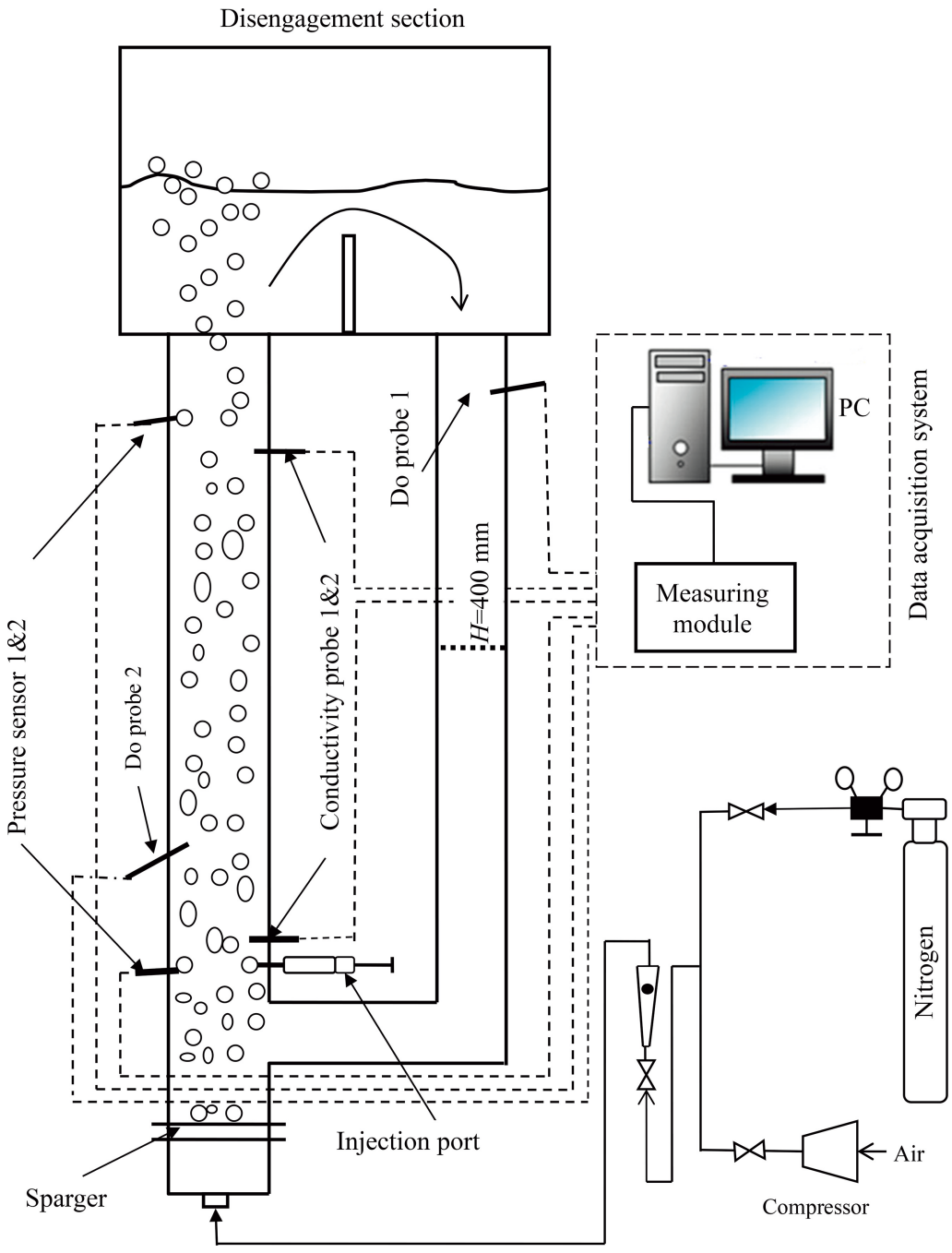


Fig. 1. Schematic diagram of external loop airlift reactor.

Table 2
Geometrical dimensions of a sectionalized external loop airlift reactor

Sr. No	Work volume/m^3	Dimension of riser ($D \times H$)/m	Dimension of downcomer ($D \times H$) /m	Height of liquid level H_L/m	Dimension of gas-liquid separator ($D \times H$)/m
1	16×10^{-3}	0.094 × 1.510	0.039 × 1.410	1.443	0.240 × 0.330

British standard pipe (BSP) male thread. They are made of two pressure probes approximately 3 mm apart, and encapsulated in Stanley Steel tubing and connected to Personal computer (PC) *via* the interface circuit.

The gas hold-up is one of the vital hydrodynamic parameters which determine the rate of mass transfer as well as liquid circulation velocity. The gas hold-up in the riser is determined using the following equation:

$$\varepsilon_G = 1 - \frac{\Delta P}{\Delta P_O} \tag{1}$$

Table 3
Set of experiments performed for in EL-ALR

Sr. No	Set. No	Gas flow rate/$m^3 \cdot s^{-1}$	Superficial gas velocity/$m \cdot s^{-1}$	Flow area of the internal and diameter of plates their details/%
1	1	1.6×10^{-5}	0.0024	(Configuration-A)
2		3.3×10^{-5}	0.0048	No Internal (0)
3		5.0×10^{-5}	0.0072	
4		6.6×10^{-5}	0.0096	
5		8.3×10^{-5}	0.012	
6		1.0×10^{-4}	0.0144	
7		1.1×10^{-4}	0.0168	
1	2	1.6×10^{-5}	0.0024	(Configuration-B) Plate 1 to 5 each plate having same flow area 16.70% (6 mm size)
2		3.3×10^{-5}	0.0048	Total number of holes are 40, apart from 24 mm
3		5.0×10^{-5}	0.0072	
4		6.6×10^{-5}	0.0096	
5		8.3×10^{-5}	0.012	
6		1.0×10^{-4}	0.0144	
7		1.1×10^{-4}	0.0168	
1	3	1.6×10^{-5}	0.0024	(Configuration-C) Total no. of holes = 30 1.6% (2 mm size) 5.4% (4 mm size)
2		3.3×10^{-5}	0.0048	12.2% (6 mm size)
3		5.0×10^{-5}	0.0072	
4		6.6×10^{-5}	0.0096	
5		8.3×10^{-5}	0.012	
6		1.0×10^{-4}	0.0144	
7		1.1×10^{-4}	0.0168	

where ΔP is the dynamic pressure which is measured by a pressure sensor located in riser section at $U_G > 0$, ΔP_O is measured static pressure at $U_G = 0$ (liquid hydrostatic head)

2.1.2. Liquid circulation velocity (V_{LC})

The conductivity monitoring system, consisting of two conductivity probes (diameter 10 mm), a conductivity meter, an analog to digital/digital to analog converter (ADC/DAC) and a computer has been used to acquire the conductivity data at a sampling frequency of 10 Hz. The locations of conductivity probes are as shown in Fig. 1. Two conductivity probes with response time less than one second are used in this work. The conductivity range 0–2.0 mS and the second range is 0–20 mS is used. They simply consist of two electrodes, approximately 3 mm apart, and encapsulated in plastic tubing, every one of them is connected to personal computer via the interface circuit. Fig. 1 shows the locations of the probes along the column and the tracer injection point.

The liquid linear velocity (v_r) in the riser sector is determined using a tracer dose method [23,24]. Two ml sodium chloride solution is added into the riser as a pulse at the injector tap using an air-driven injector system. The liquid conductivity reply is documented at two downstream locations using the same conductivity probes. The time interval between the conductivity peaks and the known vertical distance between the probes are used o determine the liquid linear velocity. The liquid linear velocity in the riser is determined by Eq. (2)

$$v_r = \frac{d_e}{t_p} \tag{2}$$

where d_e is the vertical distance between the probes and t_p is the time interval between the conductivity peaks.

$$U_{Lr} = (1 - \varepsilon_G)\, v_r \tag{3}$$

$$U_{Lr}\, A_r = U_{Ld}\, A_d \tag{4}$$

$$U_{Ld} = \frac{U_{Lr}\, A_r}{A_d} \tag{5}$$

The superficial liquid velocity in the downcomer (U_{Ld}) and riser (U_{Lr}) are determined from the Eqs. (3) and (5). The A_d and A_r are the cross-sectional areas of the downcomer and riser respectively.

2.1.3. Bubble size distribution

For bubble size distribution, images are taken using a Canon DSLR EOS 1300D camera. The size distribution is measured in the middle section of the riser in EL-ALR. To avoid curvature effects, the square box (150 mm × 110 mm) has been used. The images of bubbles are taken below and above the plate by illuminating the bubbles with diffuser backlight. The images are captured at different superficial gas velocities for plate configuration B (Plate-1) as shown in Fig. 2.The Web Plot Digitizer software is used to estimate bubble minor axis and major axes of ellipse-shaped bubbles.

The study of bubble size distribution and shapes by using image analysis is a matter of rigorous research. In the literature many researchers [25–29] have discussed that the bubble shape is totally defined by knowledge of its major axis and minor axis. In this research, each bubble is approximated and reconstructed by using ellipses. The average size of bubble is determined for the superficial gas velocity ranging from 0.0024 to 0.0168 $m \cdot s^{-1}$. The effect of bubble size distribution for different superficial gas velocity for the plate configuration B (plate −1) is as shown in Fig. 2.

The size of the bubbles (ellipse) and a number of a bubble are varying with superficial gas velocity. The equivalent diameter of the ellipse is determined by using major axis *2a* and minor axis *2b* of bubbles. The Finally equivalent diameter D_{eq} and aspect ratio are obtained as:

$$\psi = b/a \tag{6}$$

$$D_{eq} = 2\sqrt[3]{a^2 b} \tag{7}$$

$$d_{bs} = \frac{\sum_i^N n_i\, d_{Bi}^3}{\sum_i^N n_i\, d_{Bi}^2} \tag{8}$$

where d_{Bi} is the diameter of bubble classes i and n_i is the number of the bubbles of size class i respectively and n is the number of classes used for the distribution.

2.1.4. Liquid axial velocity (U_L)

The liquid axial velocity is measured by using an ultrasonic velocity profile instrument. The principal to the obtained velocity profile information is based on ultrasonic echography and doppler effect. The liquid average axial velocity is measured in downcomer at height H = 950 mm from the bottom for superficial gas velocity

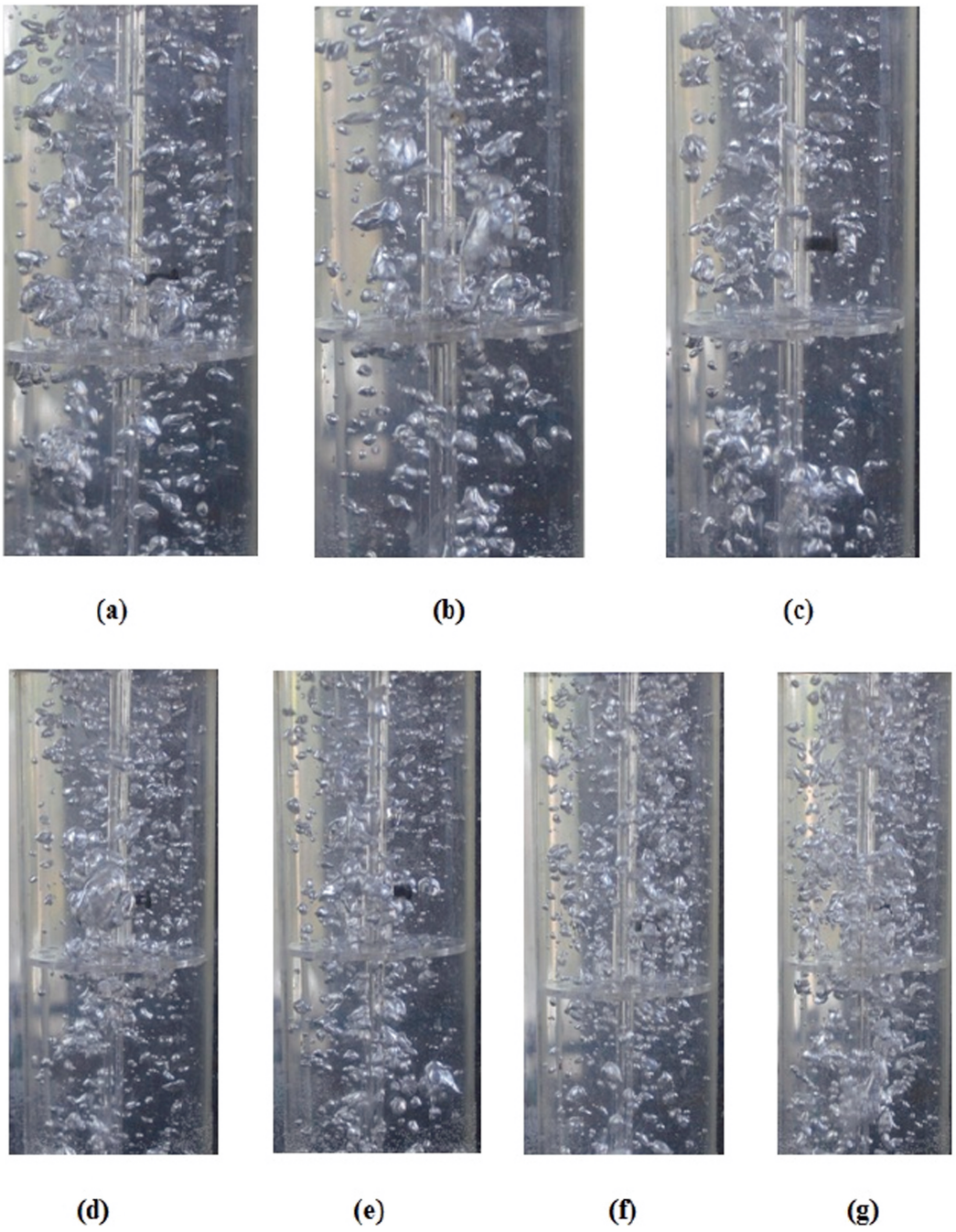


Fig. 2. For different superficial gas velocities the bubble size distribution for plate configuration-B (Plate-1) (a) 0.0024 m·s^{-1} (b) 0.0048 m·s^{-1} (c) 0.0072 m·s^{-1} (d) 0.0096 m·s^{-1} (e) 0.012 m·s^{-1} (f) 0.014 m·s^{-1} (g) 0.016 m·s^{-1}.

ranging from 0.0024 to 0.012 m·s^{-1} as shown in Fig. 1. An ultrasonic transducer is emitted pulsed ultrasonic wave propagates to the fluid inside the downcomer: Impurities and contaminations in the fluid (seeding particles for laboratory use) reflect the wave and the transducer receives the echo. Transducer device is capable of transforming an electrical signal to ultrasonic vibrations (waves). It emits these waves into media surrounding its active face. In reverse, transducer works as a receiver of ultrasonic waves and changes them to electric signals.

2.1.5. Volumetric mass transfer coefficient

The volumetric mass transfer coefficient (k_La) is measured using the graphical method. The initial oxygen concentration is reduced to zero by adding nitrogen gas. Nitrogen being inert in nature does not cause any changes to the coalescing properties of tap water. The mass balance for the dissolved oxygen in the well-mixed liquid phase can be established as

$$\frac{dC}{dt} = K_La(c^* - c) \tag{9}$$

where c is the oxygen concentration, dc/dt is concentration gradient of liquid phase, c^* is the equilibrium dissolved oxygen concentration. Some measuring methods are based on Eq. (9) and different techniques for measuring the dissolved oxygen and concentration can be used. The concentration of dissolved oxygen measured using a dissolved oxygen probe that is located at the riser and downcomer

section as shown in Fig. 1. The tip of the one probe is downward and anther upward at an angle of 20° to the horizontal prevents gas bubble adhering to the tip.

In order to calculate the volumetric mass transfer coefficient Eq. (9) is first integrated and the graph of $\ln(c^* - c/c^* - c_0)$ *vs* time is plotted.

$$\ln\left(\frac{c^* - c}{c^* - c_0}\right) = K_L a(t) \tag{10}$$

The slope of the graph is equal to the volumetric mass transfer coefficient in whole reactor.

The volumetric mass transfer coefficient is average of local mass transfer at gas-liquid interface. Such local mass transfers are expressed by governing equation of local concentration.

$$\frac{\partial_{\varepsilon_L} c_L}{\partial t} + \nabla \cdot \varepsilon_L c_L U_L = \nabla \cdot \varepsilon_L((D_m + D_t)(\nabla \cdot c_L)) + K_L a(c^* - c) \tag{11}$$

The governing Eq. (11) can be solved from analytically. The local mass transfer coefficient and diffusion in each part of reactor is accounting. The local mass transfer coefficient is determined by classical theory of mass transfer models from Section 3.4 given below. The terms accounting for molecular diffusion D_m, turbulent diffusion D_t and interfacial mass transfer in Eq. (11) can be compared with the terms of the overall Eq. (9).

We obtained following equation for the conservation average concentration:

$$\frac{\partial c}{\partial t} + U_L \frac{\partial c}{\partial Z} = D_A \frac{\partial^2 c}{\partial Z^2} + K_L a(c^* - c) \tag{12}$$

where D_A is axial dispersion coefficient, this includes molecular diffusion, turbulent diffusion and spatial dispersion. The overall mass transfer coefficient is depends on axial dispersion coefficient.

2.1.6. Power consumption (P_g)

The effect on power input for different plate configurations has been studied in the present work. The specific power input has been estimated using Eq. (13).

$$\frac{P_g}{V_{\text{total}}} = U_G \times \rho_L \times g \times (1 - \varepsilon_G) \tag{13}$$

where P_g/V_{total} is total specific power consumption and ϵ_G is a gas hold-up in the riser section. The correlation has been made for specific power consumption with bubble size distribution for plate configuration A & C.

3. Mathematical Modeling

3.1. Governing equation

The Eulerian-Eulerian multiphase model is used to simulate the hydrodynamics of flow in this study. The continuous and disperse of phases are treated as on interpenetrating media identified by their local volume fractions. The system considered a continuum and averaged transport equations are determined for each phase. The Reynolds averaged mass and momentum balance equations are solved for each of the phases.

Phasic volume fractions define the region occupied by each phase and are incorporated into the conservation equations for mass and momentum. The phase volume fraction α must satisfy the relation:

$$\sum_{k=1}^{n} \alpha_k = 1 \tag{14}$$

where n is the total number of phases. The conservation equations are written by performing a collaborative average of the local instantaneous balance for every phase. Only two phases are needed to describe gas-liquid flows, $n = 2$. The liquid is modelled as the continuous (primary) phase and gas is modelled as the dispersed (secondary) phase. CFD simulation in an external loop airlift reactor has been carried out using standard k-epsilon the model.

3.2. Continuity equation

$$\frac{\partial}{\partial t}(\rho_k \varepsilon_k) + \nabla(\rho_k \varepsilon_k u_k) = 0 \tag{15}$$

3.3. Momentum transfer equation

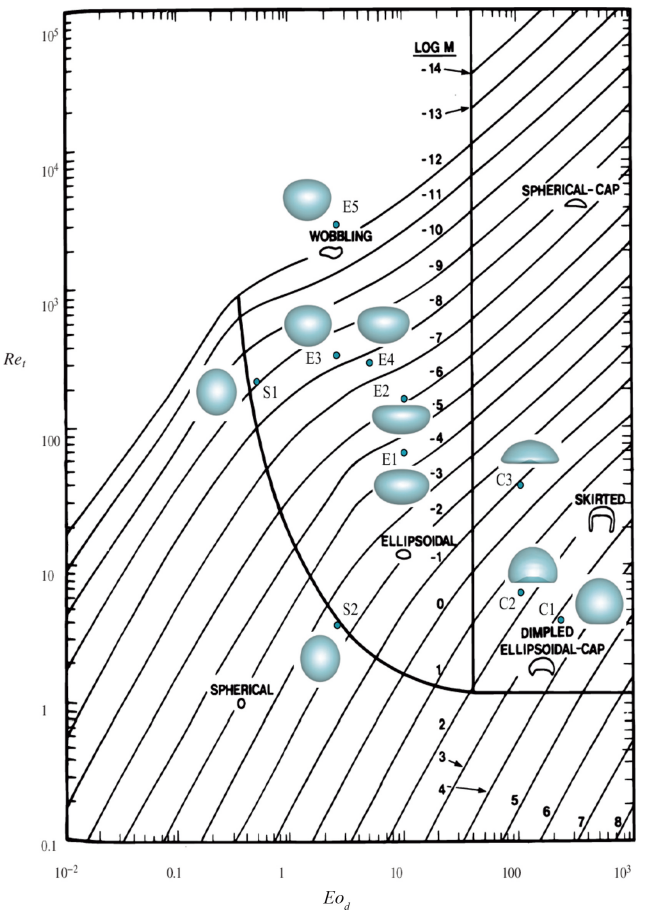


Fig. 3. Regime diagram for the shape of bubbles ascending in a quiescent fluid according to bubble shapes as a function of terminal Reynolds number Re_t, and Eötvös number Eo_d [36].

$$\frac{\partial}{\partial t}(\rho_k \varepsilon_k u_k) + \nabla(\rho_k \varepsilon_k u_k u_k) = -\nabla(\varepsilon_k \tau_k) - \varepsilon_k \nabla P + \varepsilon_k \rho_k g + M_{I,k} \tag{16}$$

Table 4
Grids description of 3D simulation

Sr. No	Mesh	Cell number	Descriptions
1	Grid-1	Grid-1 (E-1619020)	Full domain ΔX = 0.002 m Sparger ΔX = 0.002 m
2	Grid-2	Grid-2 (E-221830)	Full domain ΔX = 0.004 m Sparger ΔX = 0.002 m
3	Grid-3	Grid-3 (E- 221217)	Full domain ΔX = 0.006 m Sparger ΔX = 0.002 m
4	Grid-4	Grid-4 (E-22135)	Full domain ΔX = 0.007 m Sparger ΔX = 0.002 m

The terms on the right-hand side of Eq. (16) are representing the stress, pressure gradient, gravity and the ensemble-averaged momentum exchange between the phases. The stress term of phase k is described as

$$\tau_k = -\mu_{eff,k}\left(\left(\nabla u_k + (\nabla u_k)^{\mathrm{T}} - \frac{2}{3}I(\nabla u_k)\right)\right) \tag{17}$$

where, $\mu_{eff,k}$ is effective viscosity. The effective viscosity of the liquid phase is composed of three contributors, such as molecular viscosity, turbulent viscosity and an extra term due to bubble induced turbulence [10,11,30].

$$\mu_{eff,L} = \mu_L + \mu_{T,L} + \mu_{BI,L} \tag{18}$$

The calculation of effective gas viscosity is based on effective liquid viscosity which is as follows:

$$\mu_{eff,G} = \frac{\rho G}{\rho L}\mu_{eff,L} \tag{19}$$

Turbulence induced by the movements of bubbles can be calculated by the model proposed by Sato and Sekoguchi:

$$\mu_{BI,L} = \rho_L C_{\mu,BI}\, \varepsilon_G\, d_B\, |\mu_G - \mu_L| \tag{20}$$

With a model constant $C_{\mu,BI} = 0.6$

In order to close the system of equations, turbulent eddy viscosity has been formulated using turbulent kinetic energy (k) and turbulent energy dissipation (ϵ)

$$\mu_{T,L} = \rho_L C_\mu \frac{k^2}{\epsilon} \tag{21}$$

The turbulent kinetic energy and turbulent energy dissipation are calculated by following a governing equation

$$\frac{\partial}{\partial t}(\rho_k \varepsilon_L k) + \nabla(\rho_L \varepsilon_L u_L k) = -\nabla\left(\varepsilon_L \frac{\mu_{eff,L}}{\sigma_k}\nabla k\right) - \varepsilon_L(G - \rho_L \varepsilon_L) \tag{22}$$

The rate of dissipation of turbulent kinetic energy is calculated from its governing equation

$$\frac{\partial}{\partial t}(\rho_L \varepsilon_L \epsilon) + \nabla(\rho_L \varepsilon_L u_L \epsilon) = -\nabla\left(\varepsilon_L \frac{\mu_{L,eff}}{\sigma_\varepsilon}\nabla\epsilon\right) + C_{\varepsilon 1}\varepsilon_L \frac{\epsilon}{k}(G + C_{\varepsilon 3}G_b) - C_{\varepsilon 2}\rho_L \epsilon \tag{23}$$

The standard model parameters are considered in present simulations such as C_μ = 0.09, $C_{\varepsilon 1}$ = 1.44, $C_{\varepsilon 2}$ = 1.92, $C_{\varepsilon 3}$ = 1.3, σ_k=1.0 and σ_ε = 1.3. The term G in the above equation is related to the production of turbulent kinetic energy and described by:

$$G = \tau_L : \nabla u_L \tag{24}$$

These equations are solved by using the finite volume approach. The various correlations are used to near the system of equation.

The term momentum exchange energy interfacial force $M_{I,k}$ in Eq. (16) is represent the interaction forces between the continuous and dispersed phase. The forces acting on a motionless bubble in liquid are pressure and gravity. Since there is usually, relative motion between the bubble and liquid, the liquid flow around individual bubbles leads to local variations in pressure and shear stress. A bubble imbedded in a flowing fluid is influenced by a number of mechanisms, acting on it due to the interaction at the gas-liquid interface. The single particle is moving through fluid experience forces that affect its motion. If the slip velocity is constant, the force is called drag. If the motion is non-uniform, one needs to extend the concept of drag to include various other forces

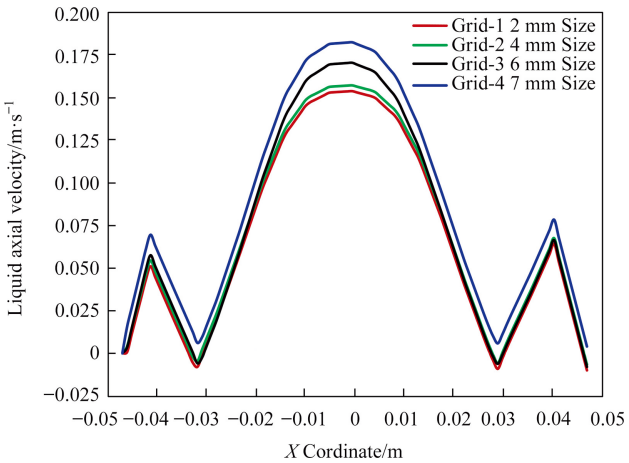


Fig. 5. Simulation results of the liquid axial velocity in riser section at H = 675 mm for superficial gas velocity 0.0072 m·s^{-1} with different grid sizes.

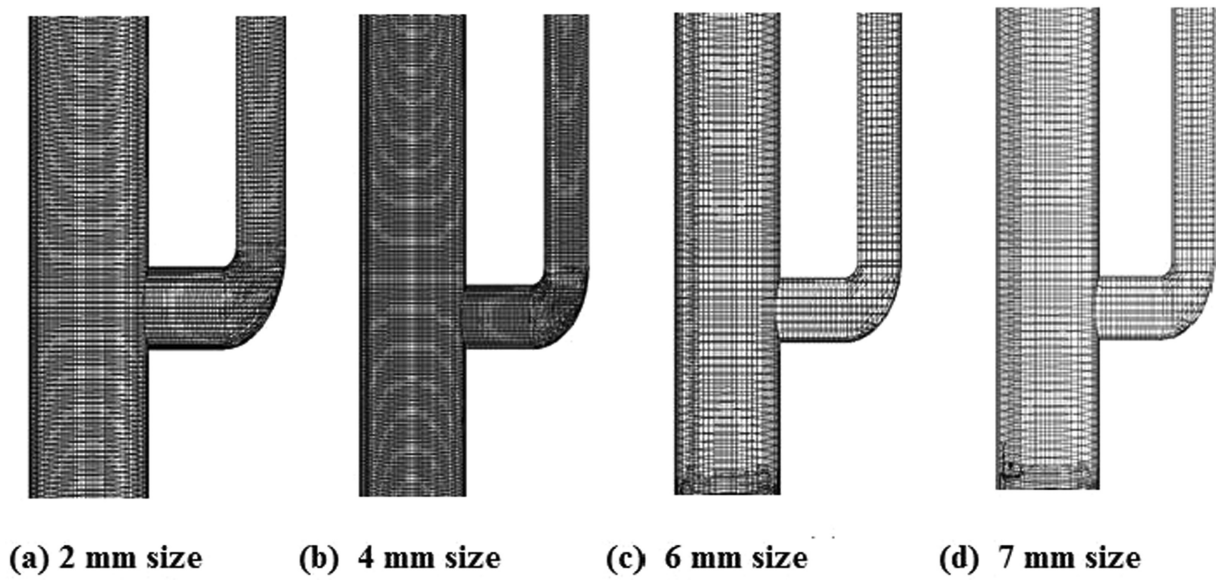


Fig. 4. Computation grid and grid sizes.

such as virtual mass force, lateral lift force, turbulent dispersion force and wall force. Therefore, the total interfacial force acting between the two phases can be formulated as

$$M_{I,L} = -M_{I,G} = M_{D,L} + M_{L,L} + M_{VM,L} + M_{TD,L} + M_{W,L} \quad (25)$$

(1) Drag force ($M_{D,L}$)

The various researchers [6,8,31] have recommended the following correlations for drag formation in two-phases flows in an external loop airlift reactor.

$$C_D = \frac{4}{3}\frac{g\, d_B}{{V_T}^2}\frac{(\rho_L - \rho_G)}{\rho_L} \quad (26)$$

where V_T is the terminal velocity

$$V_T = \frac{\mu_l\, Mo^{-0.149}(J - 0.857)}{\rho_l\, d_B} \quad (27)$$

$$J = \left\{0.094\, H^{0.757} 2 < H < 59.3\right\} \quad (28)$$

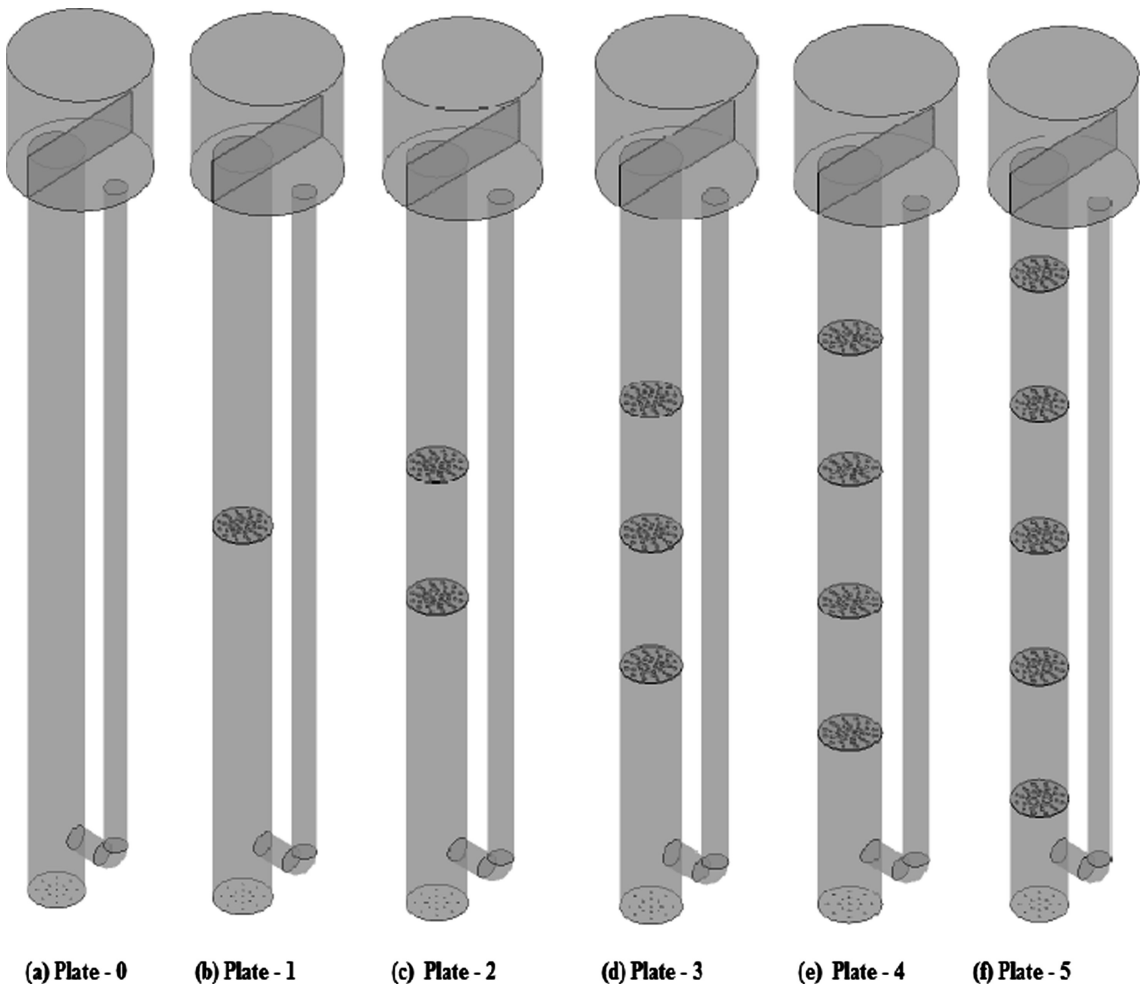


Fig. 6. CFD geometrical view of EL-ALR for plate configuration A & B.

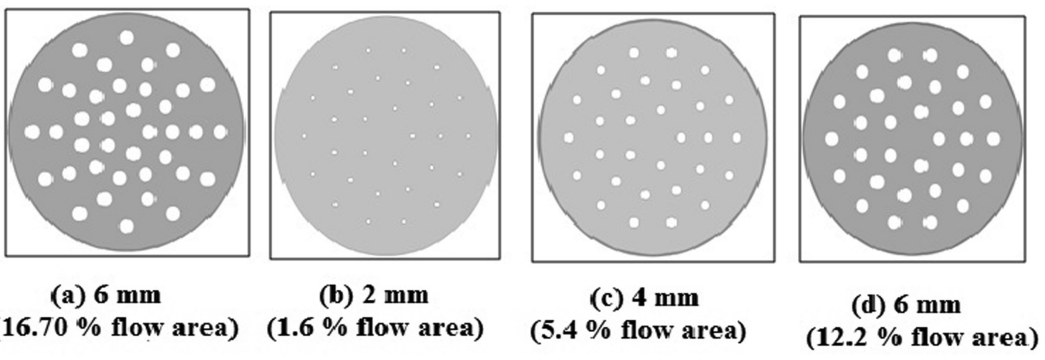


Fig. 7. Geometry of plate configuration B & C.

Table 5
Simulation settings

Multiphase model	Euler-Euler two-phase model
Viscous model	k-epsilon RSM model standard wall function
Turbulent multiphase model	Dispersed
Primary fluid	Water
Secondary fluid	Air
Boundary condition	
Inlet	Velocity inlet specified Turbulent intensity (10%) and hydraulic diameter is specified as 3 mm
Outlet	Pressure outlet Pressure is specified at atmospheric condition Backflow turbulent intensity (5%) Backflow hydraulic diameter of outlet is specified 0.24 m
Wall	No-slip condition
Bubble diameter	According to plate configuration A & B Table 8
Drag force	According to Grace Model
Non-drag force	Virtual mass coefficient was used 0.5
Lift coefficient	According to Author Tomiyama relation Eq. **(33)**.
Surface tension	Constant 0.0712 $N \cdot m^{-1}$
Solution methods	
Solution	Pressure velocity coupling Phase couple simple
Spatial discretization	
Gradient	Least squares cell-based
Momentum	First order upwing
Volume fraction	First order upwing
Turbulent kinetic energy	First order upwing
Turbulent dissipation rate	First order upwing
Superficial gas velocity	0.0024 $m \cdot s^{-1}$ to 0.0168 $m \cdot s^{-1}$
Time step	0.001 s

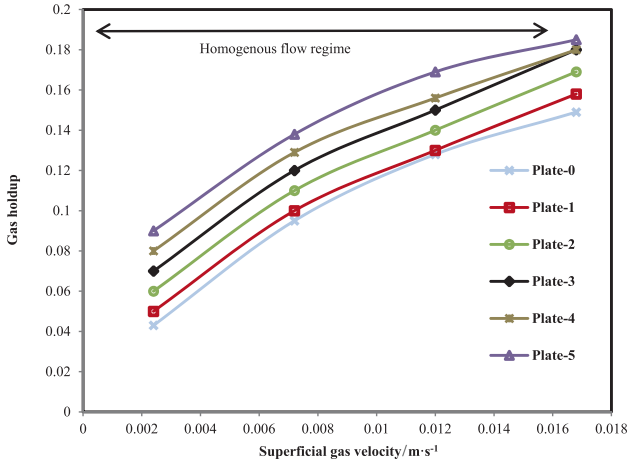


Fig. 8. Flow regime map of external loop airlift reactor with plate configuration A & B.

$$J = \left\{3.42\, H^{0.441}\ H > 59.3\right\} \tag{29}$$

$$H = \frac{4}{3} Eo\, Mo^{-0.149} \left(\frac{\mu_l}{\mu_{\text{ref}}}\right) \tag{30}$$

where, Mo is Morton number which considers physical properties of two phases.

$$Mo = \frac{{\mu_L}^4\, g\, \Delta\rho}{{\rho_L}^2\, \sigma^3} \tag{31}$$

where, σ is the surface tension between the phases. The reference kinematic viscosity is taken as $\mu_{\text{ref}} = 0.0009\ \text{kg} \cdot \text{m}^{-1} \cdot \text{s}^{-1}$.

(2) Transversal or Lateral force (Lift force) ($M_{L,L}$)

Many experimental studies suggest that lateral movement of the bubble depends on bubble size, as small bubbles tend to move towards the wall of the vessel and larger bubbles towards the centre of the vessel [32–34]. The parameters affecting the transverse force acting on a spherical bubble in shear flow are (a) relative velocity between dispersed and continuous phases; (b) shear rate of continuous phase; (c) bubble rotational speed; and (d) non-slip or slip boundary condition at bubble surface.

$$M_{L,L} = -C_L\, \rho_L\, \alpha_G\, (u_G - u_L) \times (\nabla \times u_L) \tag{32}$$

For a spherical bubble the shear lift coefficient (C_L) is positive as lift force acts in the direction of decreasing liquid velocity, *i.e.* in case of co-current pipe flow, it acts in the direction towards the pipe wall. The experimental [35] and numerical research showed that the direction of the lift force changes its sign if a substantial deformation of the bubble occurs. The lift coefficient C_L depends on the Eötvös number for a water-air system at normal conditions. The following equation was proposed in the literature [35] to determine the lift coefficient (C_L).

$$C_L = \left\{ \begin{array}{c} \min\left[0.288 \tanh\left(0.121 Re\right), f(E_{od})\right] E_{od} < 4 \\ f(E_{od}) = 0.00105 E_o^3 - 0.0159 E_{od}^2 - 0.0204 E_{od} + 0.4744 \le E_{od} \le 10 \\ -0.29 E_{od} > 10 \end{array} \right\} \tag{33}$$

where, E_{od} is a non-dimensional Eötvös number. The average size of the bubble is determined from experimental analysis for different plate configurations A, B and C.

The experimental bubble size distribution is determined for different plate configuration A and B as given in Table 8. At the low Eötvös number bubble is maintain spherical shape and moves towards the wall while at high Eötvös number it becomes deformed and moves towards the centre of the riser. The reason behind this is formation of slanted ¨vortex behind the deformed bubble causing bubble to migrate to the riser centre in an external loop airlift reactor. The relation between terminal Reynolds number, Re_t, and Eötvös number on bubble shape is already reported in the literature as shown in Fig. 3.

Table 6
Experimental and CFD predictions of gas hold-up for plate configuration-B

Sr. No	Superficial gas velocity/$m \cdot s^{-1}$	Experimental and CFD prediction of gas holdup, ε_G					
		Plate-5	Plate-4	Plate-3	Plate-2	Plate-1	Plate-0
1	0.0024	0.09 (0.08)	0.08 (0.07)	0.07 (0.06)	0.06 (0.053)	0.05 (0.041)	0.043 (0.033)
2	0.0072	0.13 (0.12)	0.12 (0.11)	0.12 (0.11)	0.11 (0.105)	0.10 (0.10)	0.095 (0.085)
3	0.012	0.16 (0.17)	0.16 (0.16)	0.15 (0.16)	0.14 (0.155)	0.13 (0.15)	0.128 (0.13)
4	0.0168	0.185 (0.19)	0.18 (0.19)	0.17 (0.18)	0.169 (0.18)	0.15 (0.17)	0.149 (0.16)

Bracket number indicate simulation results of gas hold-up.

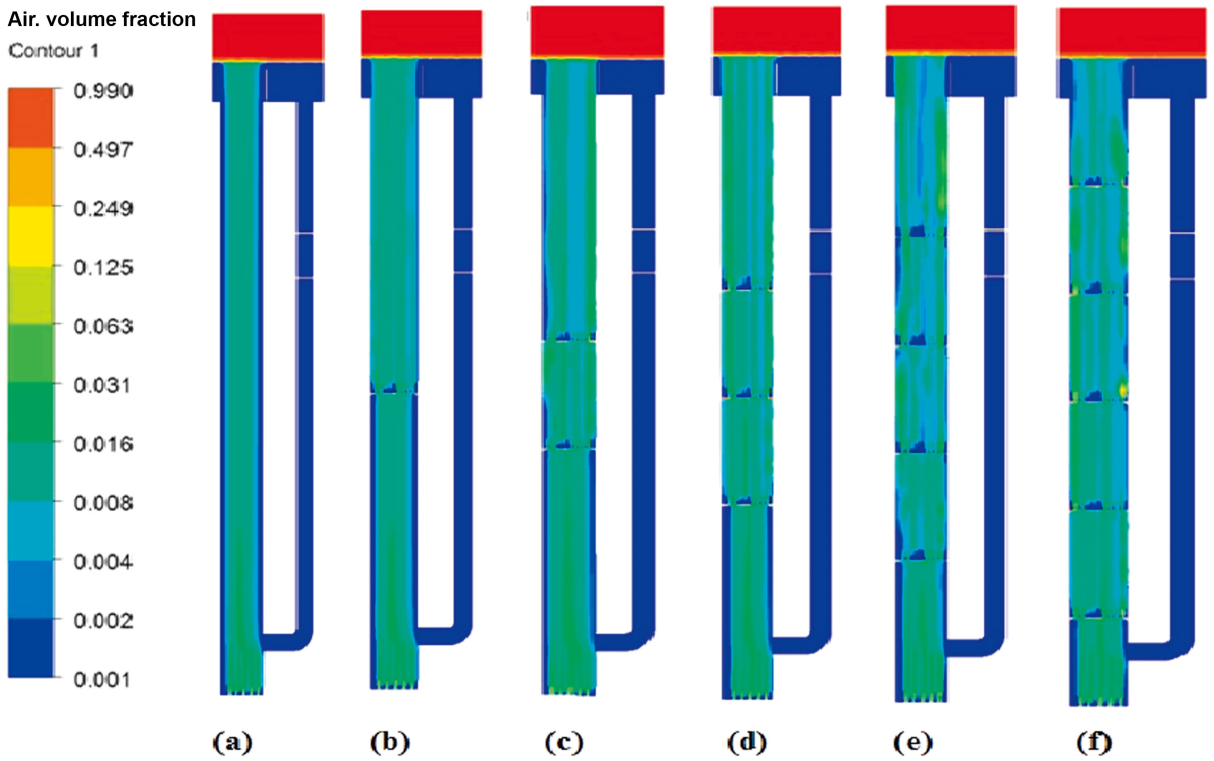


Fig. 9. Overall gas hold up contours for superficial velocity of gas U_G = 0.0024 m·s^{-1} for plate configuration A & B. (a) Plate-0 (b) Plate-1 (c) Plate-2 (d) Plate-3 (e) Plate-4 (f) Plate-5.

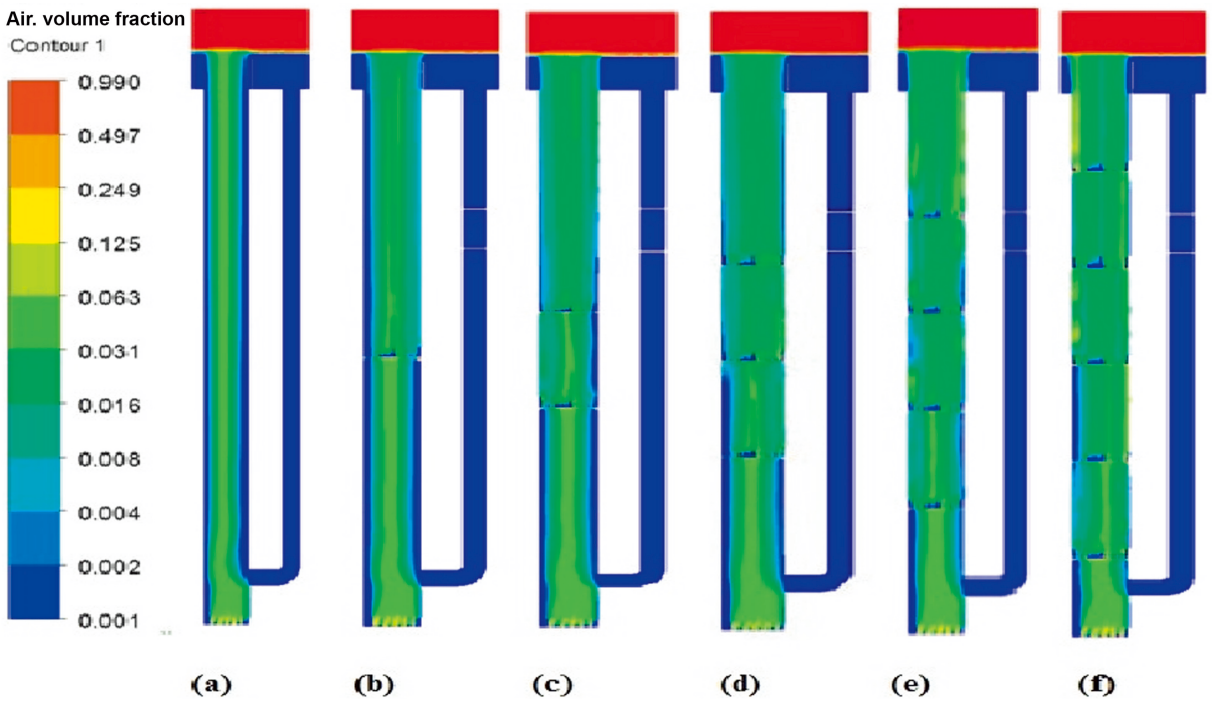


Fig. 10. Overall gas hold up contours for superficial velocity of gas U_G = 0.0072 m·s^{-1} for plate configuration A & B. (a) Plate-0 (b) Plate-1 (c) Plate-2 (d) Plate-3 (e) Plate-4 (f) Plate-5.

(3) Virtual mass force ($M_{VM.\,L}$)

When a bubble accelerates in a liquid phase, it will also accelerate the neighbouring liquid around it. The general expression for this force is developed [37] and the virtual mass force is calculated [38] by:

$$M_{VM,L} = -\varepsilon_G\,\rho_L\,C_{\mathrm{vm}}\frac{D}{D_t}(u_G - u_L) \tag{34}$$

where, the coefficient C_{vm} is added/virtual mass coefficients and it corresponds to the volume fraction of the liquid that is accelerating with the bubble. In the present simulation, the value of virtual mass coefficient is used as 0.5.

3.4. Mass transfer model

The complete volumetric mass transfer coefficient (k_La) is measured from the product of the overall mass transfer coefficient (k_L) and specific interfacial area (a_i) per unit liquid volume. The specific interfacial area (a_i) for mass transfer related to mean bubble diameter (d_B) and overall gas hold-up (ε_G) is given by a well-known equation given as

$$a_i = \frac{6\,\varepsilon_G}{d_B(1-\varepsilon_G)} \tag{35}$$

There are certain models available in the literature for computing local mass transfer coefficient (k_L) but the usually used model is based on penetration theory [39] and surface renewal model and two film models. The liquid phase mass transfer coefficient of a bubble with a movable surface is according to penetration theory by [39] represented by

$$k_L = 2\sqrt{\frac{D_l}{\pi\,t_e}} \tag{36}$$

where D_l diffusivity of oxygen in water and t_e is contact time is calculated from Kolmogorov's length scale of isotropic turbulence as calculated from ($\sqrt{t_e} = \sqrt{\nu_l/\epsilon_l}$; where ν_l kinematic viscosity of liquid and ϵ_l turbulent eddy dissipation rate. Eq. (37) becomes

$$k_L^{\mathrm{penetration}} = \frac{2}{\sqrt{\pi}}\,D_l^{0.5}\left(\frac{\epsilon_l}{\nu_l}\right)^{0.25} \tag{37}$$

The Eq. (37) model is specified as $k_L^{\mathrm{penetration}}$. The mass transfer coefficient (k_L) suggested by Danckwert [40] is given by equation $k_L = \sqrt{D_l\,s}$ Where s is a fraction of surface renewal rate. The D_l is the diffusivity of oxygen in the water. The mass transfer coefficient is related to an average surface renewal rate of bubble interface

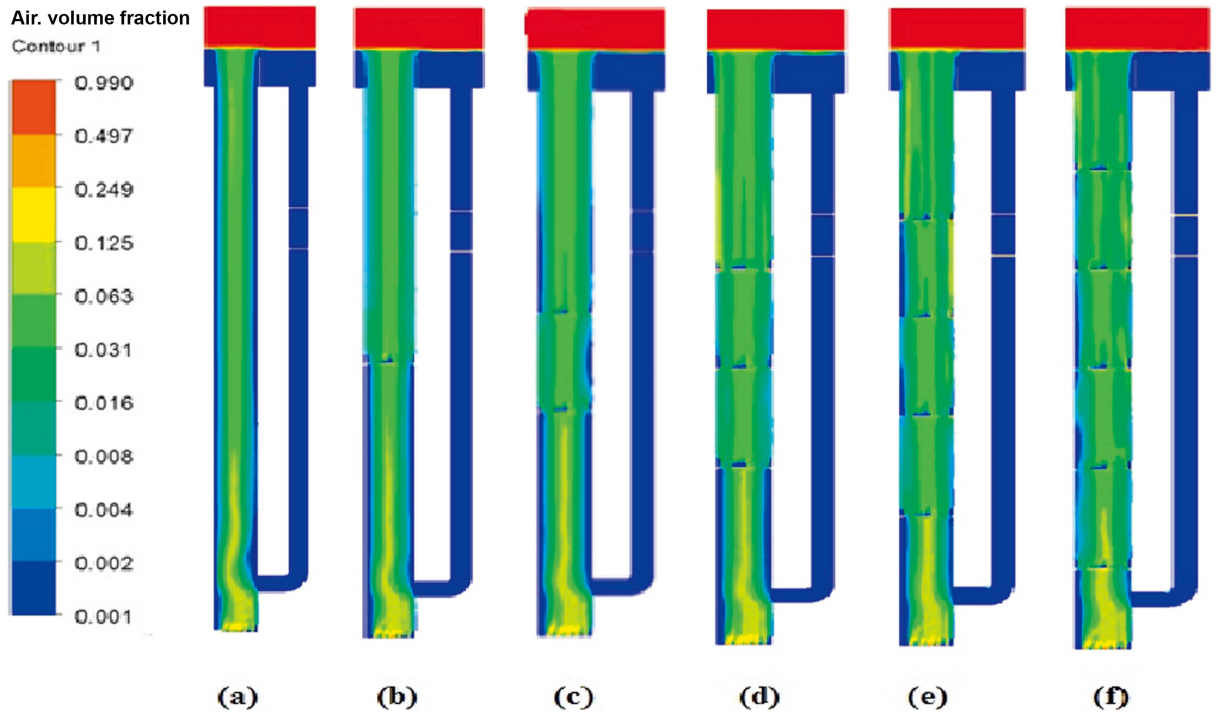


Fig. 11. Overall gas hold-up contours for superficial velocity of gas U_G = 0.012 m·s^{-1} for plate configuration A & B. (a) Plate-0 (b) Plate-1 (c) Plate-2 (d) Plate-3 (e) Plate-4 (f) Plate-5.

Table 7
Experimental and CFD predictions of liquid circulation velocity for plate configuration-B

Sr. No	Superficial gas velocity/m·s^{-1}	Experimental and CFD prediction of liquid circulation velocity, U_{Lr} /m·s^{-1}					
		Plate-5	Plate-4	Plate-3	Plate-2	Plate-1	Plate-0
1	0.0024	0.23 (0.22)	0.25 (0.24)	0.33 (0.32)	0.35 (0.34)	0.50 (0.51)	0.72 (0.732)
2	0.0072	0.36 (0.35)	0.46 (0.45)	0.61 (0.60)	0.93 (0.94)	1.17 (1.18)	1.27 (1.28)
3	0.012	0.51 (0.50)	0.88 (0.87)	1.11 (1.12)	1.79 (1.80)	2.16 (2.20)	2.29 (2.309)
4	0.0168	0.85 (0.82)	1.72 (1.73)	2.15 (2.16)	2.72 (2.71)	2.94 (2.99)	3.0 (3.09)

Bracket number indicate simulation results of liquid circulation velocity.

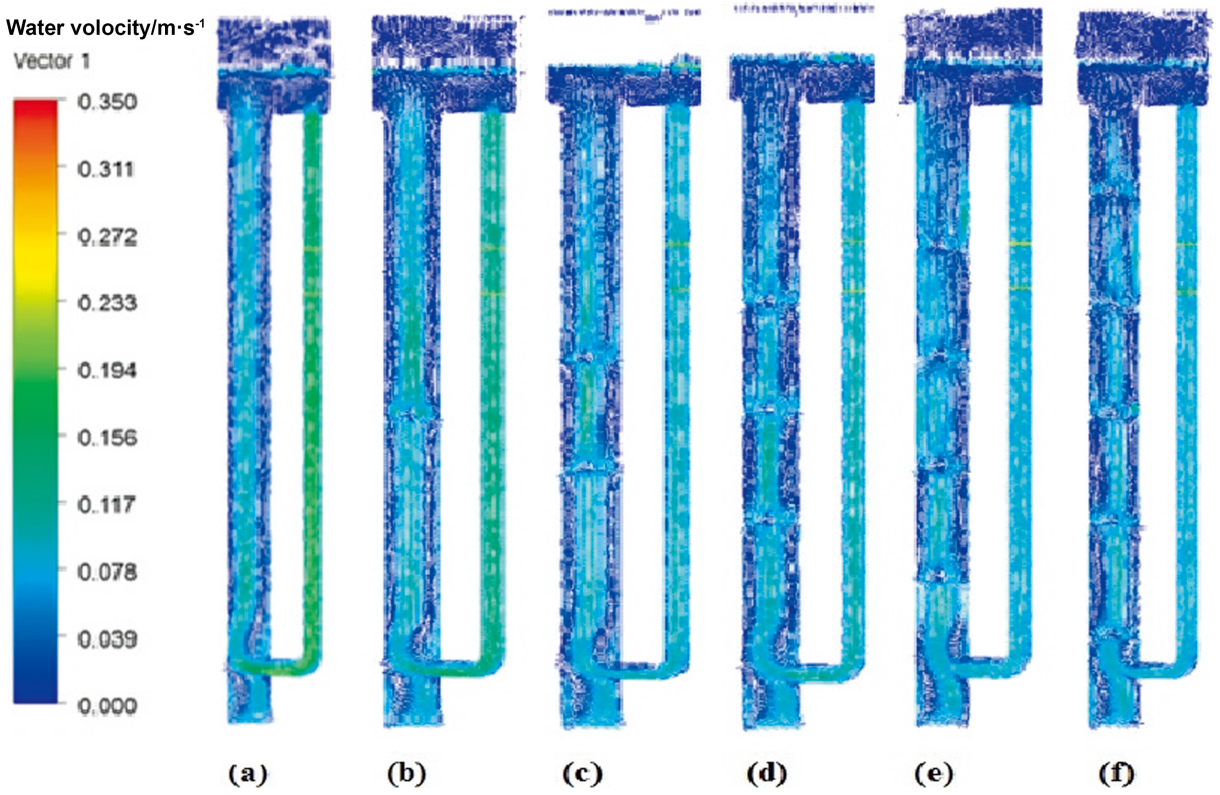


Fig. 12. Liquid circulation velocity vector for superficial velocity of gas U_G = 0.0024 m·s^{-1} for Plate configuration A & B. (a) Plate-0 (b) Plate-1 (c) Plate-2 (d) Plate-3 (e) Plate-4 (f) Plate-5.

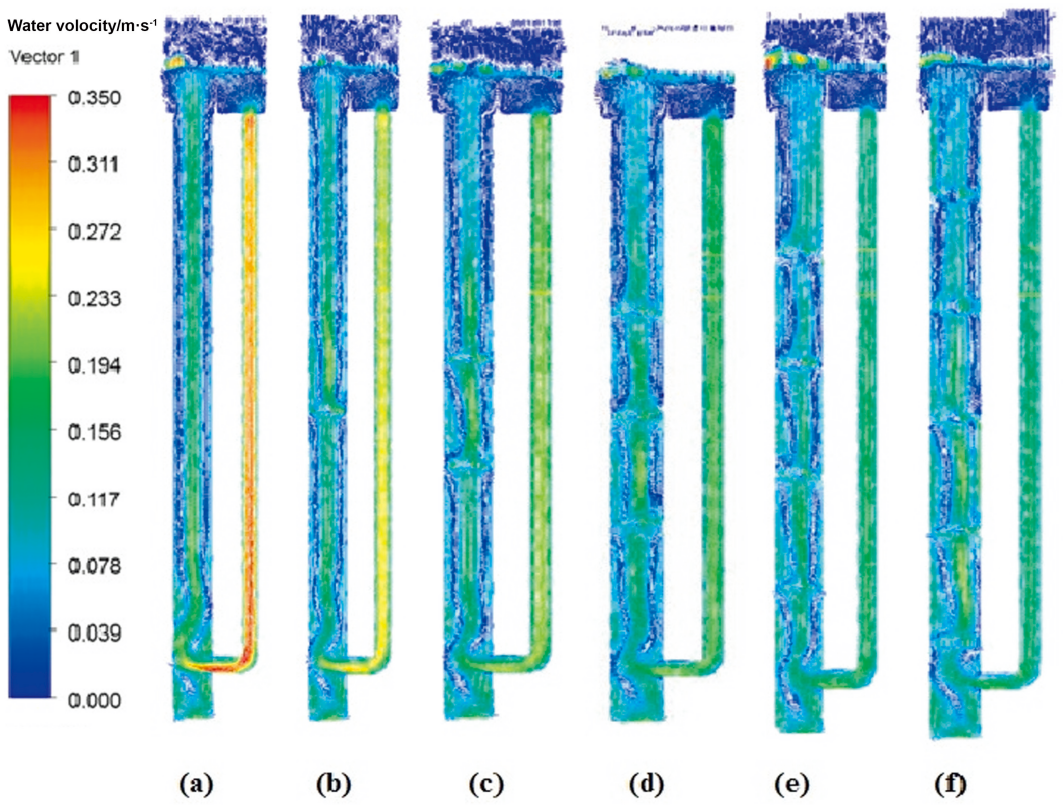


Fig. 13. Liquid circulation velocity vector for superficial velocity of gas U_G = 0.0072 m·s^{-1} for plate configuration A & B. (a) Plate-0 (b) Plate-1 (c) Plate-2 (d) Plate-3 (e) Plate-4 (f) Plate-5.

between eddies with variable contact time. The mass transfer coefficient (k_L) so suggested by many researchers based upon a theory of isotropic turbulence is given by

$$k_L^{\text{eddy cell}} = KD_l^{0.5}\left(\frac{\epsilon_l}{\upsilon_l}\right)^{0.25} \tag{38}$$

The Eq. (38) model is signified as $k_L^{\text{eddy cell}}$ and usually referred to as the eddy cell model. Where D_l is the oxygen diffusivity in water υ_l is the dynamic viscosity of a liquid ε_l is turbulent eddy dissipation rate and k = 0.4 (model constants).

$$k_L^{\text{slip velocity}} = \frac{2}{\sqrt{\pi}}\sqrt{\frac{D_l\, U_{\text{slip}}}{d_B}} \tag{39}$$

where U_{slip} is slip velocity of two phases (gas and liquid). Which can be determined by a difference in gas-liquid velocity from CFD simulation. In Ref. [41] modified the equation of mass transfer coefficient (k_L) based on bubble rigidity and is signified as k_L^{rigid} and this is achieved from the equation suggested by [42] boundary value theory based on laminar flow.

$$k_L^{\text{rigid}} = C\left(\frac{U_{\text{slip}}}{d_B}\right)^{0.5} D_l^{2/3}\nu_l^{-1/6} \tag{40}$$

where C is constant taken equal to 0.6 and ν_l is the kinematic viscosity of water. The volumetric mass transfer coefficient (k_La) is determined by using a mass transfer coefficient of different models and specific interfacial area (a) which was determined from Eq. (35). The graphical method is used to determine the experimental volumetric mass transfer coefficient and already described in previous Section 2.1.5. The experimental volumetric mass transfer coefficient for different plate configurations A and B are compared with different mass transfer models discussed in the next section.

3.5. Computational grid

The grid convergence studies are carried out for verifying the grid independence of the solution. The number of grid nodes in the X, Y, and Z direction in the external loop airlift reactor are shown in Table 4. The four grids are generated which comprises of 1,619,020 (Grid-1), 221,830 (Grid-2), 221,217 (Grid-3) and 22,135 (Grid-4) elements respectively. The finer grid is employed near the sparger region so that the strong velocity gradients in the flow can be addressed accurately. The meshing and different grid sizes are generated as shown in Fig. 4. The liquid axial velocity is calculated in the riser section at H = 675 mm height from the bottom and the superficial gas velocity 0.0072 m·s^{-1} is used. In comparison of liquid axial velocity for grid size of 1,619,020 (Grid-1) and 221,830 (Grid-2) it shows that a similar result liquid axial velocity is obtained as shown in Fig. 5 Hence, 221,830 (Grid-2) is adapted for further simulation, which eventually decreases computational cost and time for the simulation.

3.6. Numerical solution

The non-commercial software of computational fluid dynamics ANSYS FLUENT 14.0 is used to perform CFD simulations. The geometry of EL-ALR and for different plate configuration B & C are generated and illustrated in Figs. 6 and 7. The High-resolution discretization scheme is used to discretize partial differential equations. The finite volume method is adopted to solve the equations. The simulation is carried out using the unsteady state approach.

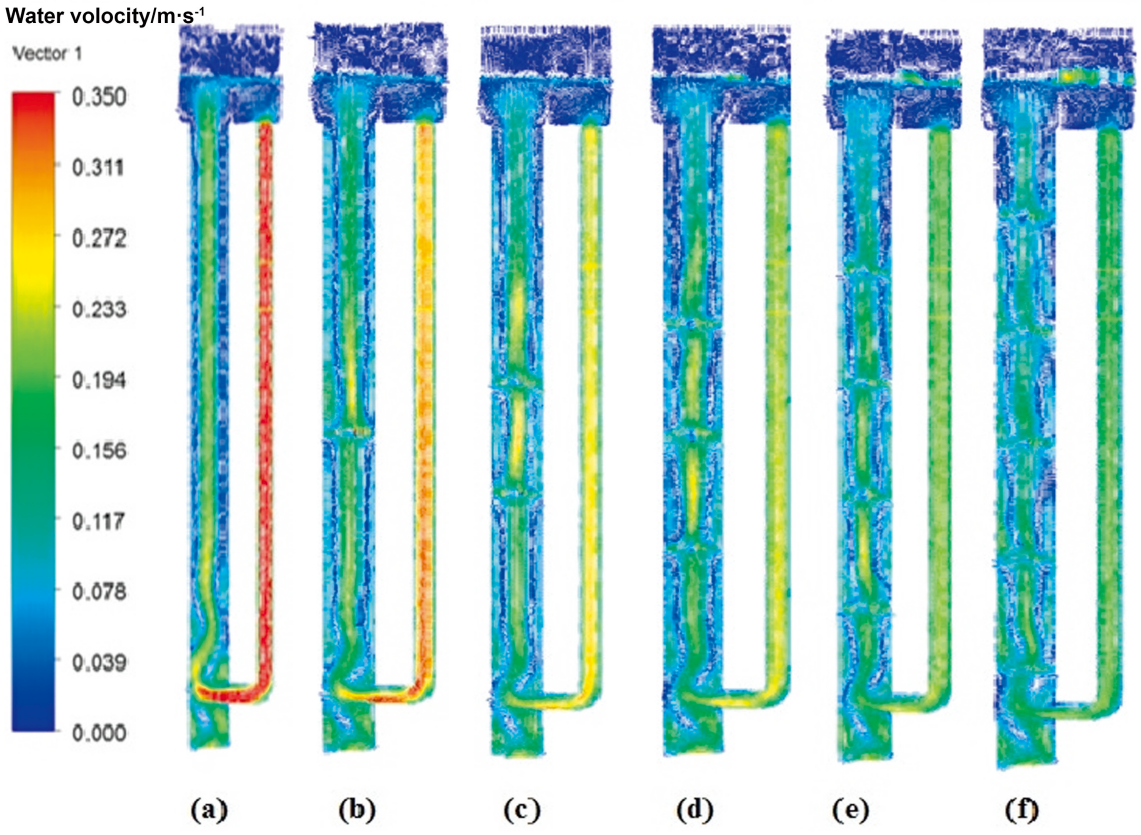


Fig. 14. Liquid circulation velocity vector for Superficial velocity of gas U_G = 0.0120 m·s^{-1} for plate configuration A & B. (a) Plate-0 (b) Plate-1 (c) Plate-2 (d) Plate-3 (e) Plate-4 (f) Plate-5.

Pressure-velocity coupling is done by using a Semi-Implicit Method for Pressure Linked Equations (SIMPLE) algorithm. The top surface of the sparger under the EL-ALR is defined as a velocity inlet. Degassing boundary condition is used to model the top surface of the reactor such that gas is only allowed to escape the reactor, not the liquid allowed. At the EL-ALR wall, no-slip boundary condition appears. In all the simulations, an air dispersed phase density of 1.225 $kg{\cdot}m^{-3}$ and viscosity of 1.7894×10^{-5} $kg{\cdot}m^{-1}{\cdot}s^{-1}$ are used and water continuous phase density of 998.2 $kg{\cdot}m^{-3}$ and viscosity of 1.003×10^{-3} $kg{\cdot}m^{-1}{\cdot}s^{-1}$ are used. The average bubble size diameters are determined from experimental for different superficial gas velocities ranging from 0.0024 $m{\cdot}s^{-1}$ to 0.0168 $m{\cdot}s^{-1}$. This measured value of the bubble diameter is then used for carrying out simulations. The effective bubble diameters are then set according to the experimental data. Each simulation step has taken 0.001 s for maximum of 20 iterations. The convergence criterions for all transport equation are set as 1×10^{-5}. The simulation settings are given in Table 5.

4. Results and Discussion

4.1. Effect of internal on gas hold-up

The flow regime is very important to flow structure, or distribution of one fluid phase relatively to the other in external loop airlift reactor. The flow regime is used to scale up of external loop airlift reactor. We have used drift-flux model of Zuber and Findlay (1969) is reported in the literature [43] for identification of flow regime in external loop airlift reactor. (i) A homogeneous bubbly flow, the bubbles rise individualistically in riser without merging with one another. This regime exists over the approximate gas velocity range, $U_G < 0.0168$ $m{\cdot}s^{-1}$, where the gas hold-up increases continuously with increase in gas velocity. (ii) A transition flow regime which is shifting of flow regime from homogenous to the heterogeneous regime. Plume velocity slowly converts from into a straight line to oscillating nature in this regime. The rate of increase in gas hold-up with increasing gas flow velocity is much lower than in the

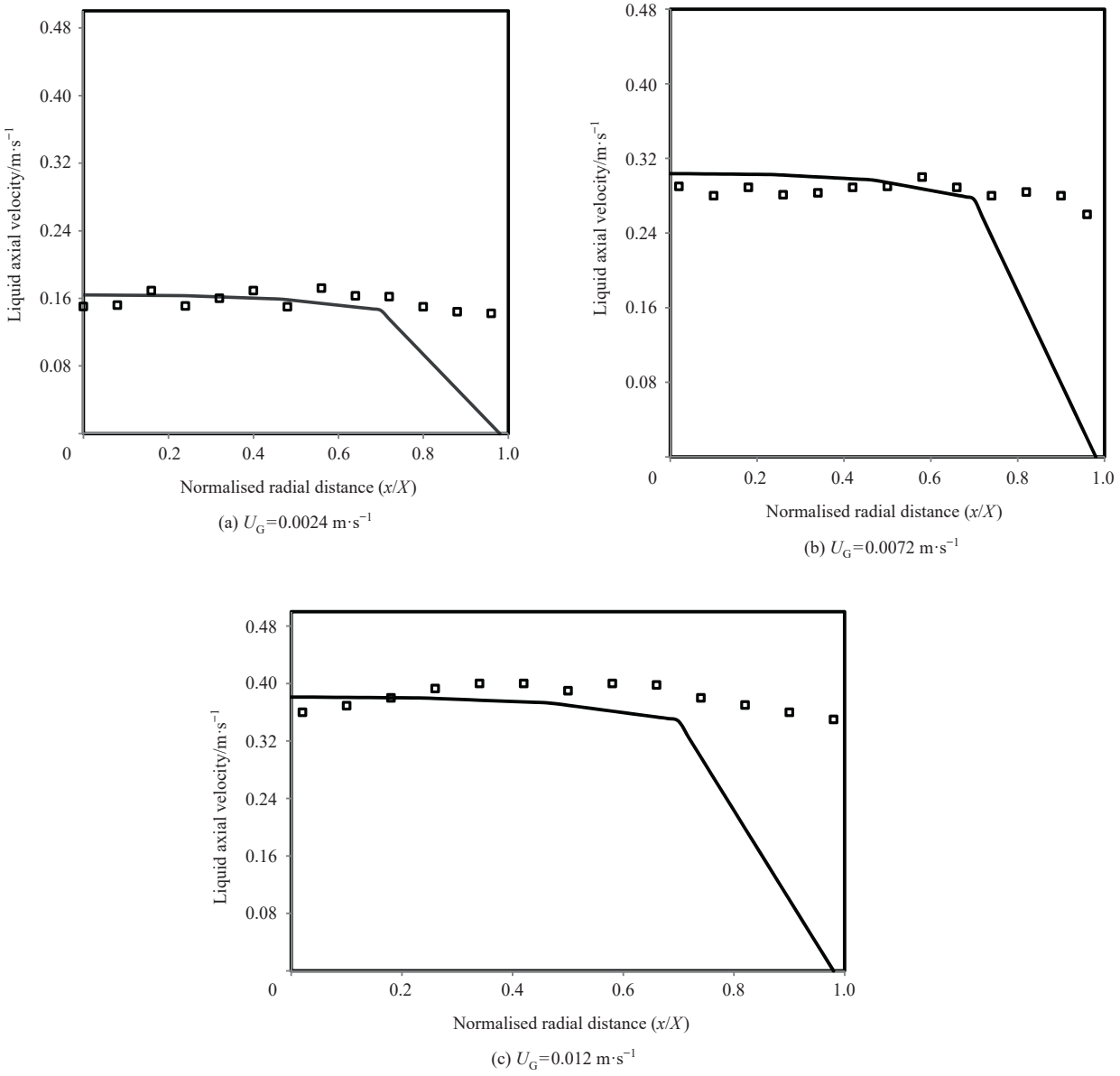


Fig. 15. Experimental and simulation result of liquid axial velocities in dowancomer at height (H = 950 mm) for different superficial gas velocity for plate configuration A.

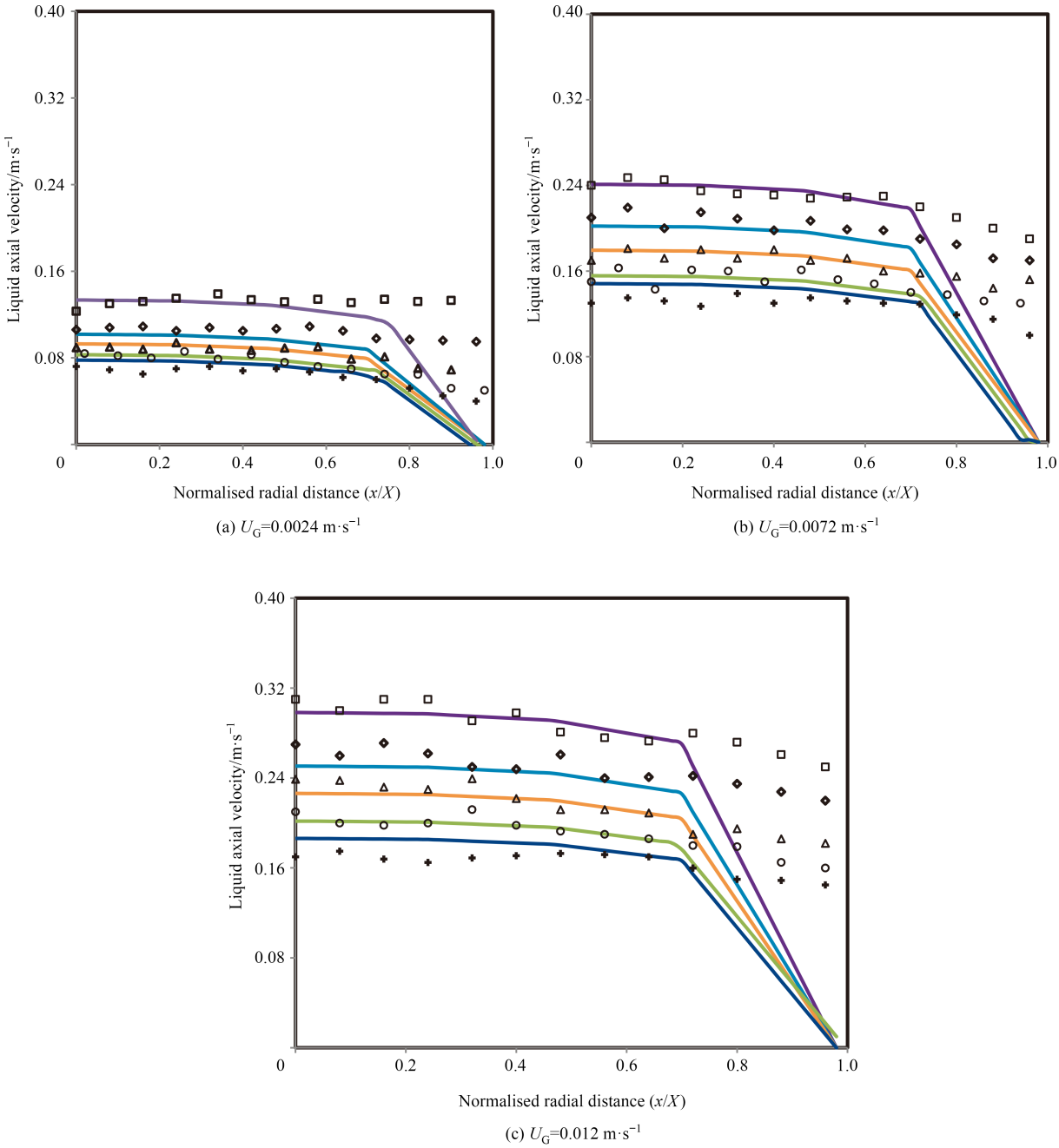


Fig. 16. Experimental and simulation result of liquid axial velocities in dowancomer at height (H = 950 mm) for different superficial gas velocity & plate configuration B. (1) Plate-1 (□) (2) Plate-2 (◇) (3) Plate-3(Δ) (4) Plate-4 (○) (5) Plate-5 (+).

bubbly flow regime (iii) the fully developed heterogeneous flow (U_G > 0.020 m·s^{-1}) involves gas flow in riser section where plume is more oscillating due to superficial gas velocity & the concentration of bubbles increases and coalescence begins. The experimental gas hold-up is determined for different plate configurations.

In the present work experiment is performed under the condition of homogenous flow regime. The superficial gas velocity is used from 0.0024 to 0.0168 m·s^{-1}. The biological processes are shear sensitive and may not withstand harsh turbulent conditions at higher superficial gas velocities. The dissolved gas concentration requirement for bioprocesses in limited and depends on the uptake by the microorganisms. Hence lower gas velocities suffice these applications. Hence the operating range of gas velocities has been chosen on lower side. The flow regime map of external loop airlift reactor with plate configuration A & B as shown in Fig. 8.

The 3D CFD simulation is conducted and validated with experimental results of gas hold-up. It can be seen from Table 6, the experimental and CFD prediction of the gas hold-up is in good agreement. From experimental studies, it has been observed that air bubbles are deposited below each internal plate as shown in Fig. 2. The air volume fraction can be seen from CFD simulation on the centre of the XY plane in a reactor for superficial gas velocity (U_G = 0.0024, 0.072, and 0.0120 m·s^{-1}). The air volume fraction is found to be more below each of the plate in sectionalized EL-ALR

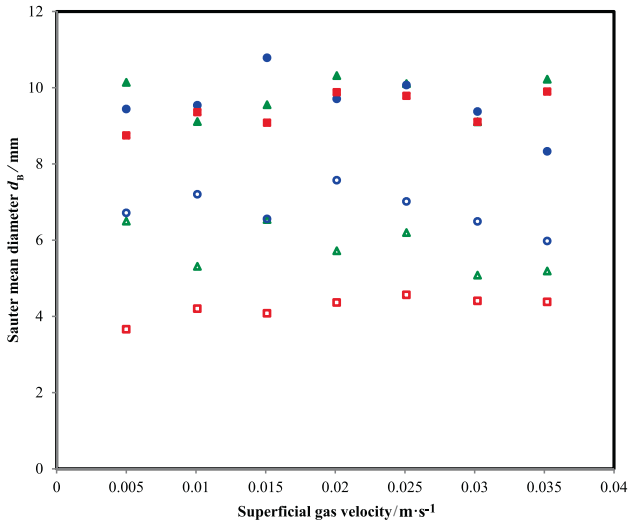


Fig. 17. Sauter mean bubble diameter *vs.* superficial gas velocity for plate configuration C. (1) 2 mm hole plate below (■) (2) 2 mm hole plate above (□) (3) 4 mm hole plate below (▲) (4) 4 mm hole plate above (△) (5) 6 mm hole plate below (●) (6) 6 mm hole plate above (○).

as shown in Figs. 9–11. Plate configurations A to B also showed increased air volume fraction as shown in Table 6.

4.2. Effect of internal on liquid circulation velocity

The liquid circulation velocity is one of the greatest significant parameters for the proper design and operation of airlift reactors. The experimental liquid circulation velocity is determined from tracer techniques & the measuring method is discussed in the previous Section 2.1.2. An increase in liquid circulation velocity resulted in an increase in superficial gas velocity for plate configuration A (no internal) and for plate configuration B, it is seen that an increase in superficial gas velocity from 0.0024 to 0.0120 m·s^{-1} resulted in decreases of overall circulation velocity also shown in Table 7. From simulations data, it is observed that by adding plates from 0 to 5, liquid circulation velocity decreases with internal plate configuration A & B as shown in Figs. 12–14. It has been observed from Table 7, predicted and experimental liquid circulation velocities are in good agreement. From the CFD simulation of each compartment in sectionalized EL-ALR, liquid circulations have been observed as shown in Figs. 12–14. The overall liquid circulation velocity depends upon the percentage flow area of each plate. From CFD simulation above the sparger plate, liquid plume velocity is observed in the range of U_G = 0.072 to 0.0120 m·s^{-1} for plate configuration A (No internal). Plume velocity is not observed in plate

Table 8
Experimental bubble size distributions for different superficial gas velocity for plate configuration A & B

Sr. No	Superficial gas velocity, U_G/m·s^{-1}	Average bubble size for plate configuration-A/m	Average bubble size for plate configuration-B/m				
		Plate-0	Plate-1	Plate-2	Plate-3	Plate-4	Plate-5
1	0.0024	0.0094	0.008	0.0069	0.006	0.0053	0.0047
2	0.0048	0.0095	0.0083	0.0073	0.0065	0.0058	0.0052
3	0.0072	0.01	0.0086	0.0071	0.0059	0.005	0.0043
4	0.0096	0.0097	0.0086	0.0077	0.0069	0.0062	0.0057
5	0.012	0.01	0.0085	0.0073	0.0063	0.0055	0.0049
6	0.0144	0.0093	0.0079	0.0067	0.0058	0.0051	0.0045
7	0.0168	0.0083	0.0071	0.0061	0.0054	0.0047	0.0042

Table 9
Sauter mean bubble diameter correlation for the plate configuration A & C

Plate configuration A & C	Range of bubble diameter/m	Correlation
Configuration – A Plate 0 (No internal)	0.0094 – 0.0083	$d_B = 0.0109(P_g/V_{total})^{-0.0322}$
Configuration – C Plate 2 mm size holes	0.0036 – 0.0043	$d_B = 0.002753(P_g/V_{total})^{-0.101}$
Plate 4 mm size holes	0.0065 – 0.0051	$d_B = 0.0084(P_g/V_{total})^{-0.0908}$
Plate 6 mm size holes	0.0067– 0.0059	$d_B = 0.008(P_g/V_{total})^{-0.037}$

Table 10
Mass transfer model comparison for sample superficial gas velocity U_G = 0.0072 m·s^{-1} for plate configuration A & B

Plate configuration	CFD simulation, $k_L \times 10^3$/m·s^{-1}				d_B/m	Specific interfacial area/m^2·m^{-3}
	Penetration model	Eddy cell model	Slip velocity model	Rigid cell model		
A						
Plate-0	1.9	0.12	0.84	0.158	0.01	68
B						
Plate-1	2.1	0.13	0.8	0.15	0.0086	90
Plate-2	1.9	0.12	0.92	0.17	0.0071	107
Plate-3	2.1	0.13	1	0.2	0.0059	127
Plate-4	2	0.12	0.91	0.17	0.005	145
Plate-5	2.3	0.14	0.94	0.17	0.0046	173

configuration B due to internal plates as shown in Fig. 12 (b-f) to 14 (b-f).

4.3. Effect of internal on liquid axial velocity

Experimental liquid axial velocity has been determined from ultrasonic velocity profile (UVP) Instrument. The measuring method is discussed in the previous section. The liquid axial velocity is measured in a downcomer in sectionalized EL-ALR at elevation of 400 mm as shown in Fig. 1. The liquid flow in the downcomer section is downward at elevation (H = 400 mm) higher due to gravity. The superficial gas velocity ranging from 0.0024 to 0.012 $m \cdot s^{-1}$ is used and it is seen from experimental studies that liquid axial velocity is higher at the centre region and low near-

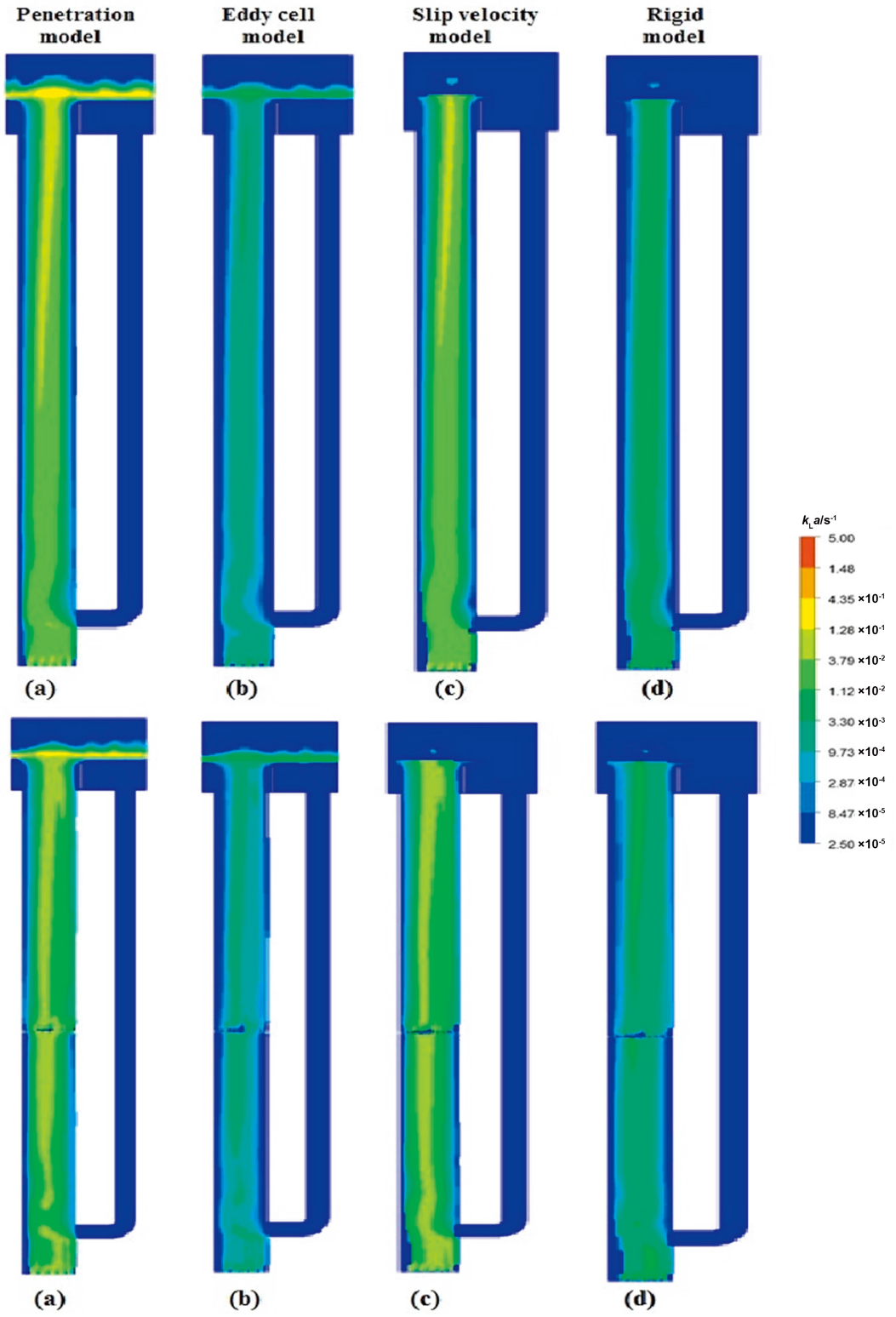


Fig. 18. Contours of liquid phase volumetric mass transfer coefficient ($k_L a$) obtained from CFD simulation for different mass transfer models. (a) Penetration model (b) Eddy cell model c) Slip velocity model (d) Rigid model for plate 0 & 1 configuration (A & B) for different bubble diameter.

wall region. The liquid axial velocity is compared for plate configurations A & B as shown in Figs. 15 and 16. It has been observed that liquid axial velocity decreases due to sectionalisation by adding plates. In addition, CFD simulation has shown that liquid axial velocity totally depends upon the overall liquid circulation velocity in the reactor. The effect of sectionalisation on overall liquid circulation reduce due to sectionalisation. It has been observed that k-epsilon models shows good agreement between experimental and prediction of liquid axial velocity. similar observation regarding the good prediction of axial liquid velocity and fractional gas

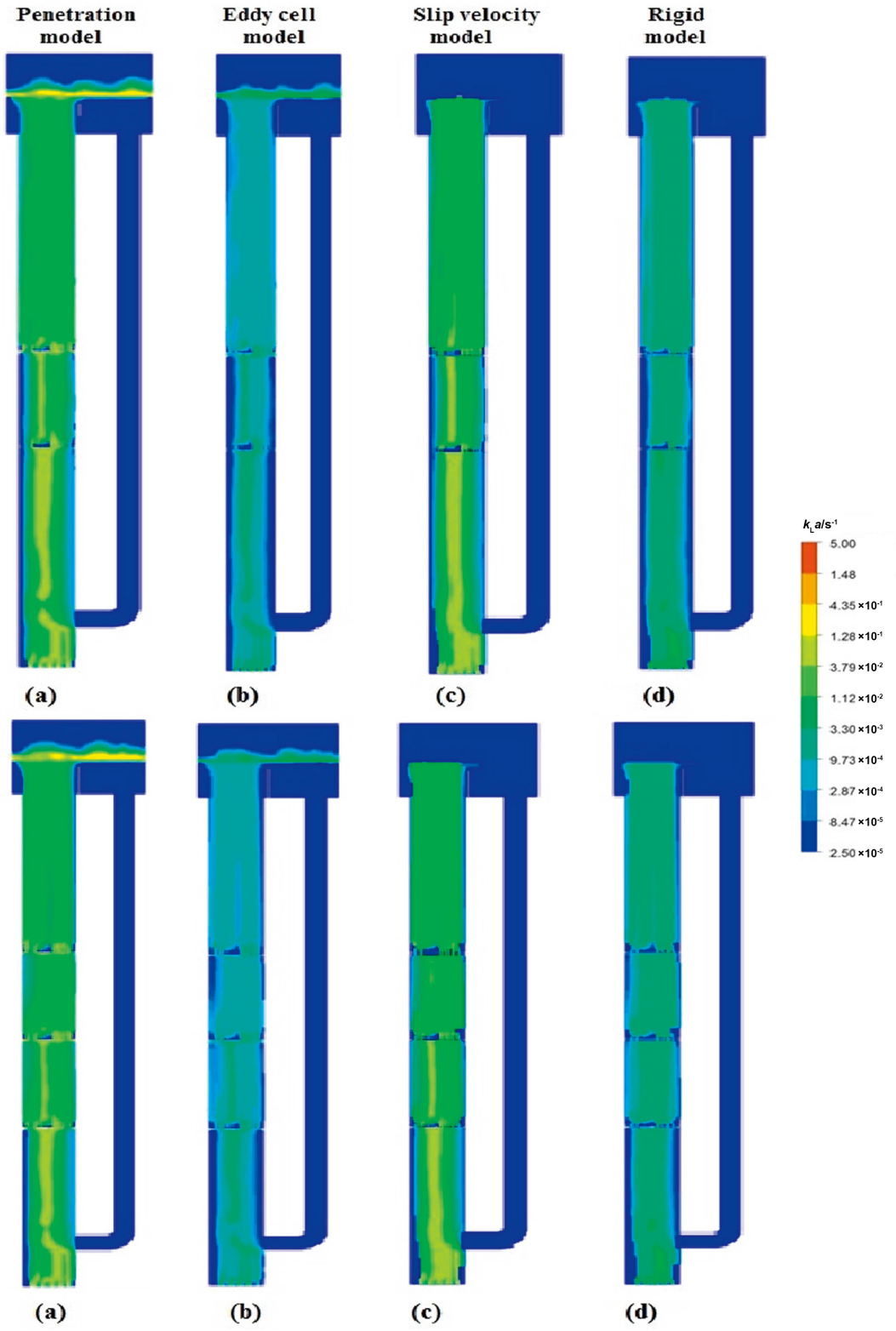


Fig. 19. Contours of liquid phase volumetric mass transfer coefficient (k_La) obtained from CFD simulation for different mass transfer models. (a) Penetration model (b) Eddy cell model (c) Slip velocity model (d) Rigid model for plate 2 & 3 configurations (B) for different bubble diameter.

hold-up using the k-epsilon model is reported in the literature and as shown in Table 1. The results are shown in Figs. 15 and 16, *i.e.* excellent agreement between CFD predictions and the experimental data for the liquid axial velocity.

4.4. Effect of internal on the bubble size distribution

The experimental method to determine bubble size distribution in sectionalized EL-ALR is already discussed. Sample photos of the actual bubble size distribution for superficial gas velocity (U_G = 0.0024–0.016 m·s^{-1}) are shown in Fig. 2. The geometry of different plate configurations are as shown in Fig. 7. In plate configuration C (2 mm hole Plate, 4 mm hole Plate, 6 mm hole Plate) the bubble size distribution has been determined for both, above & below plate as shown in Fig. 17. The plate configurations A & B are used to determine and compare average bubble size distribution when superficial gas velocity is ranging from 0.0024 to 0.0168 m·s^{-1}. The experimental average bubble size is determined

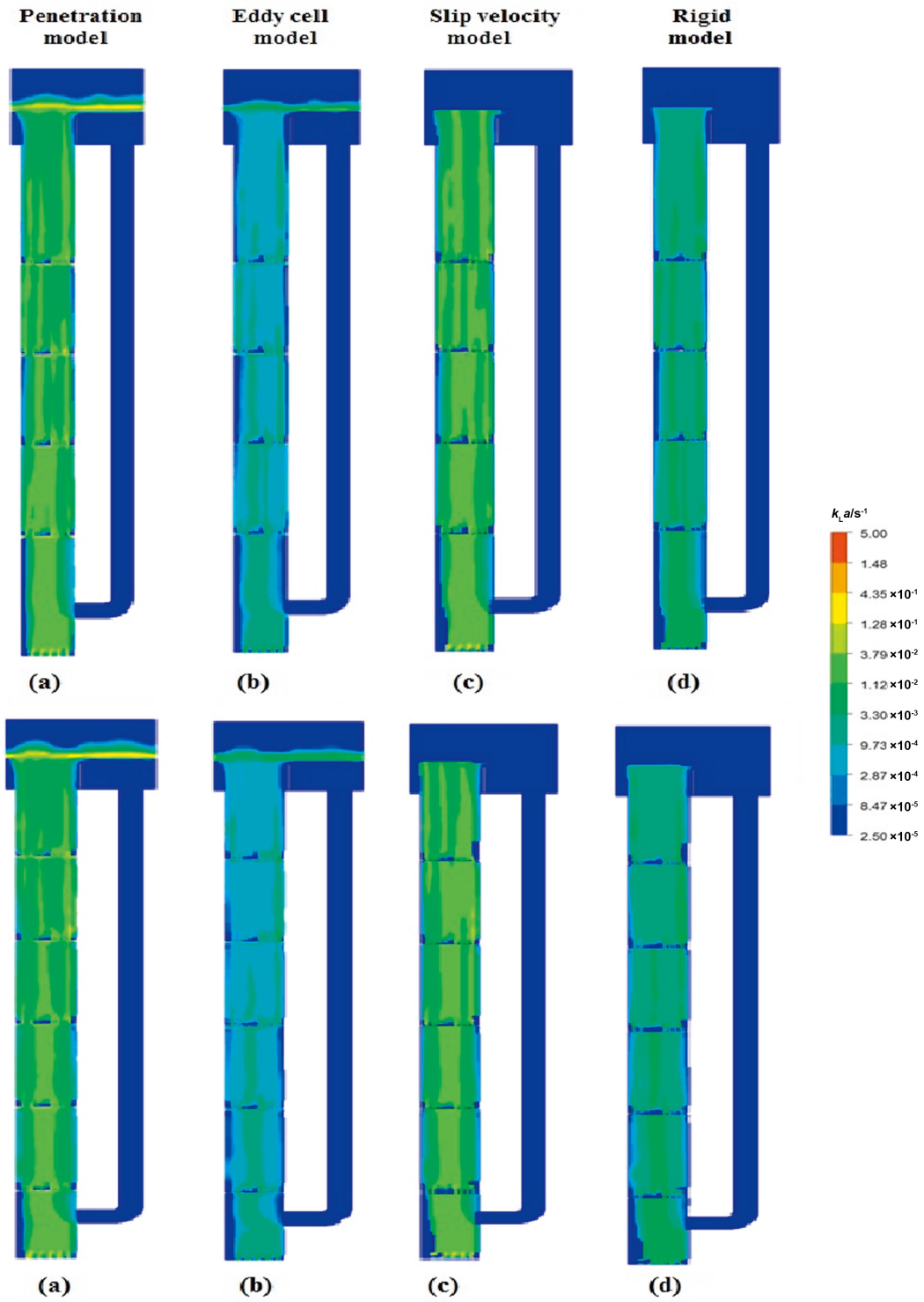


Fig. 20. Contours of liquid phase volumetric mass transfer coefficient ($k_L a$) obtained from CFD simulation for different mass transfer models. (a) Penetration model (b) Eddy cell model (c) Slip velocity model (d) Rigid model for plate 4 & 5 configurations (B) for different bubble diameter.

for plate configuration B. In plate configuration B, each plate has same flow area and by adding number of plates from 1 to 5 average size of the bubble decreases as shown in Table 8. Experimental average bubble size data is used in CFD simulation for prediction of gas hold–up, liquid circulation velocity and liquid axial velocity in sectionalized EL-ALR. The correlation for Sauter means bubble diameter and specific power consumption is determined for plate configuration A & C as shown in Table 9.

$$d_B = \widehat{a}\left(\frac{P_g}{V_{total}}\right)^{\widehat{b}} \quad (41)$$

The variation of Sauter means bubble diameter is shown in Fig. 17 for plate configuration- C. It has been observed that Sauter means bubble diameter in EL-ALR with perforated Plates configuration-A decrease with increases of specific power dissipation as shown in Fig. 17. In plate configuration C with 2 mm hole plates, the Sauter mean bubble diameter slightly increases with increase of total specific power consumption, whereas for 4 mm plate and 6 mm plate it increases with total specific power consumption increases 2 mm plate produce majority of bubbles (approximately 70 %) with diameter 0.0036 to 0.0043 m. The bubble size decreases with the size of the opening on the plate (2 mm, 4 mm and 6 mm holes size of plates) as shown in Fig. 7.

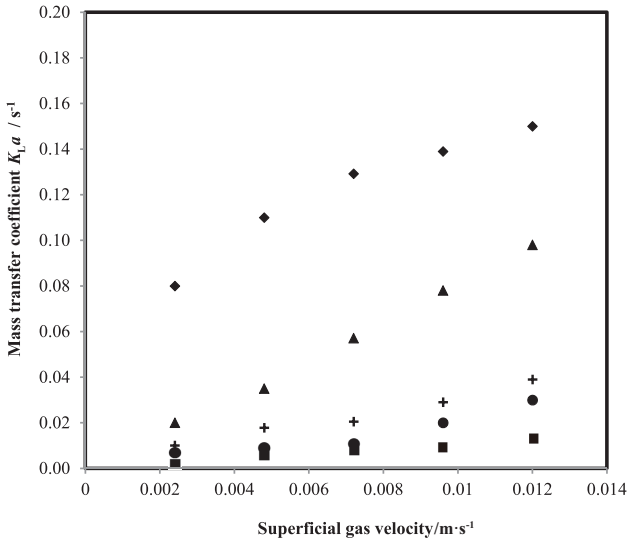


Fig. 21. Comparison of experimental and predicted of volumetric mass transfer coefficient for different mass transfer coefficient model. (◆) Penetration model (■) Eddy cell model (▲) Slip velocity model (●) Rigid cell model (+) Experimental with plate configuration A.

4.5. Prediction of mass transfer coefficient

Superficial gas velocity values are used in the range from 0.024 to 0.012 m·s^{-1} for the prediction of the mass transfer coefficient using different models. All models of mass transfer coefficient

(Penetration model, eddy cell model, slip velocity model, rigid model) have been compared for plate configuration A and B at U_G = 0.0072 m·s^{-1} and results are as shown in Table 10. It has been observed that the penetration and slip velocity model predict higher values of mass transfer coefficient as compared to other two models. Eddy cell model and rigid model showed fair agreement between experimental and simulated results therefore. These models can be accepted as the final model for the estimation of k_L. The penetration and eddy cell model does not give a significant difference in the values of k_L for an increase in plate no from 1 to 4, in the case of configuration B as shown in Table 10. The experimental bubble size is determined for plate configuration A, B and these bubble size used in the simulation. A decrease in the bubble size is observed from 0.010 m to 0.046 m from plate no 0 to 5 (configuration A to B). The interfacial area available for mass transfer also increases (68–173 m^2·m^{-3}) on increasing plate no for 0–5 plates (configuration A to B) as shown in Table 10.

The sample contours of volumetric mass transfer coefficient (k_La) at superficial gas velocity U_G = 0.0072 m·s^{-1} are determined for plate configuration A & B and are shown in Figs. 18–20. It has been also observed that the penetration and slip velocity model gives higher results of the mass transfer coefficient than the other two models.

Fig. 21 shows experimental and simulated data obtained from the CFD (using Eqs. (37)–(40)) for plate configuration A. As shown in Fig. 21, the predicted data obtained from Eqs. (38) and (40) are in good agreement with the experimental data; however, some deviations are observed between two. The predicted data obtained from Fig. 21. From Fig. 21 showed large deviations from experimental data as shown in Fig. 21. From Fig. 21 shows that the rigid cell model predicts mass transfer coefficient more effectively than other models, for plate configuration A. therefore, it has been obvious to use rigid cell model for further calculation of mass transfer coefficient from CFD simulation for plate configuration B.

The Fig. 22 shows a comparison between experimental and CFD estimated volumetric mass transfer coefficient for the plate configuration B. The volumetric mass transfer coefficient from CFD simulation and experimental data are in good agreement for plate no 1 to 5 in configuration (B). In comparison with different mass transfer model, rigid cell model gives better predictions of the mass transfer coefficient in the sectionalized external loop airlift reactor. In an external loop airlift reactor with the internal, random and irregular movement of liquid bulk films and vigorous fluctuations increased mass and momentum transfers. With the existence of internal in an EL-ALR increase in a gas hold-up and decrease liquid circulation velocity is observed. Due to low liquid circulation velocity, residence time for bubbles increases inside the sectionalized section of the riser which finally increased the mass transfer. According to the current research, for plate configuration B, overall volumetric mass transfer coefficient increased from 0.005 to 0.045 s^{-1} at the superficial gas velocity from 0.0024 to 0.012 m·s^{-1}.

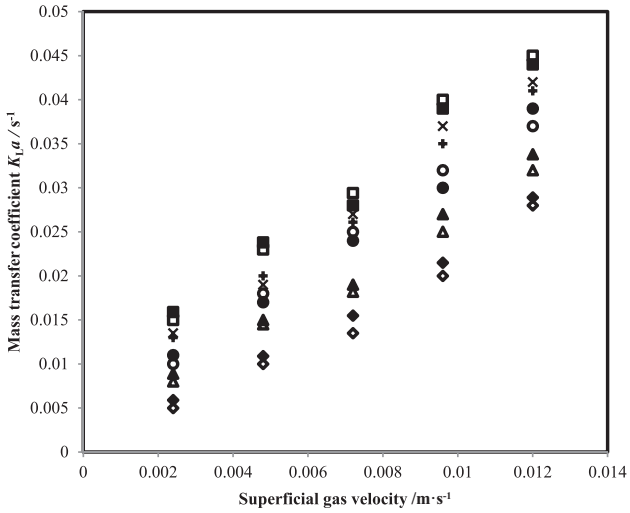


Fig. 22. Comparison of experimental and CFD predicted of volumetric mass transfer coefficient. Plate-01 (exp ◆) (CFD ◇) Plate-02 (exp ▲) (CFD Δ) Plate-03 (exp ●) (CFD ○) Plate-04 (exp ×) (CFD +) Plate-05 (exp ■) (CFD □) for plate configuration B.

5. Conclusions

Experimental and simulation result of total gas hold-up is increased with superficial gas velocity for plate number from 1 to 5. It has been observed that for plate configuration B gas hold up increases with the increases superficial gas velocity and the liquid circulation velocity decreases with increases number of plates. Each circulation section in the riser acts as continuous stirred tank reactor and has given good conversion than a single plug flow reactor. Experimentally, average bubble size is determined for plate configuration C and its effect on bubble size has been observed. It is found that initially, average bubble size is large and then it decreases with increases in superficial gas velocity. The correlation has been made in terms of average bubble diameter and specific power consumption for plate configuration C. Experimental and predicted values have shown good agreement. The CFD tools are used to predict flow patterns in a sectionalized external loop airlift reactor. The volume fraction of gas and liquid, average circulation velocity and axial liquid velocity are determined at various locations of the downcomer.

Declaration of Competing Interest

The authors declare that they have no known competing financial interests or personal relationships that could have appeared to influence the work reported in this paper.

Acknowledgements

I would like to thank Gharda Institute of Technology and Institute of Chemical Technology providing me with the fund for doing my project. I am also thankful to GIT for providing me for CFD facility I am also grateful to workshop superintendent Mr. A.S Desai and Prof P.V Jadhav for helping me with the design of External loop airlift reactor at lab scale.

Nomenclature

A_d	cross-sectional area of downcomer, m^2
A_r	cross-sectional area of riser, m^2
a	minor axis of a bubble, m
ai	specific interfacial area, $m^2 \cdot m^3$
$\widehat{a}$	empirical constant values Eq. (39)
b	major axis of a bubble, m
$\widehat{b}$	empirical constant values Eq. (39)
c^*	equilibrium dissolved oxygen concentration, $mol \cdot m^{-3}$
c	oxygen concentration, $mol \cdot m^{-3}$
c_0	initial oxygen concentration, $mol \cdot m^{-3}$
C_D	drag coefficient
C_L	lift coefficient
c_L	concentration of liquid, $mg \cdot l^{-1}$
C_{vm}	added/virtual mass coefficients
C_μ, $C_{\varepsilon 1}$, $C_{\varepsilon 2}$	constant
σ_K, σ_s	constant
d_{Bi}	diameter of bubble class I, m
D_l	diffusivity of oxygen in water, $m \cdot s^{-1}$
D_m	molecular diffusion coefficient, $m \cdot s^{-1}$
D_t	turbulent diffusion coefficient, $m \cdot s^{-1}$
D_A	axial dispersion coefficient, $m \cdot s^{-1}$
d_e	vertical distance between the probes, m
d_B	diameter of bubble, m
d_{bs}	sauter mean bubble diameter, m
G	production turbulent kinetic energy, $m^2 \cdot s^{-2}$
G	acceleration due to gravity, $m \cdot s^{-2}$
$M_{I,L}$	interfacialforcesforliquid, N
$M_{I,G}$	interfacialforcesforgas, N
$M_{D,L}$	dragforce, N
$M_{L,L}$	liftforce, N
$M_{VM,L}$	virtualmassforce, N
$M_{TD,L}$	turbulentdispersionforce, N
$M_{W,L}$	walllubricatingforce, N
ni	number of the bubbles of size class I,
P_g	power consumption, w
ΔP	dynamic pressure, psi
ΔP_O	static pressure, psi
k_L	local mass transfer coefficient, $m \cdot s^{-1}$
K_L	overall mass transfer coefficient, $m \cdot s^{-1}$
$K_L a$	volumetric mass transfer coefficient, s^{-1}
s	fraction of surface renewal rate, s^{-1}
S_K	turbulent kinetic energy dissipation rate added term, $kg \cdot m^{-1} \cdot s^{-4}$
t_p	time between the conductivity peaks, s
t	time, s
t_e	contact time of gas and liquid, s
U_L	axial liquid velocity, $m \cdot s^{-1}$
U_{slip}	slip velocity of two phases, $m \cdot s^{-1}$
U_G	superficial velocity of gas, $m \cdot s^{-1}$
U_{Ld}	superficial liquid velocity in the downcomer, $m \cdot s^{-1}$
U_{Lr}	superficial liquid velocity in the riser, $m \cdot s^{-1}$
V_r	linear velocity of liquid, $m \cdot s^{-1}$
V_{1total}	dispersion volume of gas, m^3
V_T	terminal rise velocity of a bubble, $m \cdot s^{-1}$
V_{LC}	liquid circulating velocity, $m \cdot s^{-1}$
ε_G	gasholdup
ε_L	liquidholdup
ρ_L	densityofliquid, $kgÂ \cdot m^{-3}$
ρ_G	densityofgas, $kgÂ \cdot m^{-3}$
μ_L	viscosityofliquid, $PaÂ \cdot s$
μ_W	viscosityofwater, $PaÂ \cdot s$
$\mu_{L.eff}$	effectiveviscosityofliquid, $PaÂ \cdot s$
σ	surface Tension, $NÂ \cdot m^{-1}$
v_t	turbulentviscosity, $kgÂ \cdot m^{-1}Â \cdot s^{-1}$
v_l	kinematic viscosity of liquid, $m^2 \cdot s^{-1}$
ε_l	turbulent eddy dissipation rate, $m^2 \cdot s^{-3}$
Ψ	aspect ratio

References

[1] M. Popović, C.W. Robinson, The specific interfacial area in external-circulation-loop airlifts and a bubble column-I. Aqueous sodium sulphite solution, *Chem. Eng. Sci.* 42 (1987) 2811–2824.
[2] M.Y. Chisti, B. Halard, M. Moo-Young, Liquid circulation in airlift reactors, *Chem. Eng. Sci.* 43 (1988) 451–457.
[3] M.Y. Chistit, M. Young, Airlift reactors: characteristics, applications and design considerations, *Chem. Eng. Commun.* 60 (1987) 195–242.
[4] M.Y. Chisti, Airlift Bioreactor, 1 edition., Elsevier Applied Biotechnology Series, Elsevier Applied Science, London, 1989.
[5] C. Bentifraouine, C. Xuereb, J.P. Riba, Effect of gas liquid separator and liquid height on the global hydrodynamic parameters of an external loop airlift contactor, *Chem. Eng. J.* 66 (1997) 91–95.
[6] C. Lu, Experiment and CFD simulation on gas holdup characteristics in an internal loop reactor with external liquid circulation, *Int. J. Chem. React. Eng.* 7 (2009) 1.
[7] N. Moudoud, R. Rihani, F. Bentahar, J. Legrand, Global hydrodynamic of hybrid external loop airlift reactor: Experiments and CFD modelling, *Chem. Eng. Process. - Process Intensif.* 129 (2018) 118–130.
[8] Z. Chen, Z. Jiang, X. Zhang, J. Zhang, Numerical and experimental study on the CO_2 gas-liquid mass transfer in flat-plate airlift photobioreactor with different baffles, *Biochem. Eng. J.* 106 (2016) 129–138.
[9] S.B. Pawar, CFD analysis of flow regimes in airlift reactor using Eulerian-Lagrangian approach, *Can. J. Chem. Eng.* 95 (2017) 420–431.
[10] S. Roy, M.T. Dhotre, J.B. Joshi, CFD simulation of flow and axial dispersion in external loop airlift reactor, *Chem. Eng. Res. Des.* 84 (2006) 677–690.
[11] S. Roy, J.B. Joshi, CFD study of mixing characteristics of bubble column and external loop airlift reactor, *ASIA-PACIFIC J. Chem. Eng.* 3 (2008) 97–105.
[12] K.M. Dhanasekharan, J. Sanyal, A. Jain, A. Haidari, A generalized approach to model oxygen transfer in bioreactors using population balances and computational fluid dynamics, *Chem. Eng. Sci.* 60 (2005) 213–218.
[13] J. Karcz, M. Musia, M. Bitenc, M. Doma, CFD Modelling of the fluid flow

characteristics in an external-Loop air-lift reactor, *Chem. Eng. Trans.* 32 (2013) 1435–1440.
[14] D. Law, F. Battaglia, Numerical simulations for hydrodynamics of air-water external loop airlift reactor flows with bubble break-up and coalescence effects, *J. Fluids Eng.* 135 (2013) 8.
[15] D. Law, F. Battaglia, T.J. Heindel, Simulating gas-liquid flows in an external loop airlift reactor, *ASME Int. Mech. Eng. Congr. Expo. Proc.* 10 (2009) 395–403.
[16] A.B. Pandit, Y.K. Doshi, Mixing time studies in bubble column reactor with and without internals, *Int. J. Chem. React. Eng.* 3 (2005) 1.
[17] S.N. Palaskar, J.K. De, A.B. Pandit, Liquid phase RTD studies in sectionalized bubble column, *Chem. Eng. Technol.* 23 (2000) 61–69.
[18] H. Jin, Y. Lian, L. Qin, S. Yang, G. He, Z. Guo, Parameters measurement of hydrodynamics and CFD simulation in multi-stage bubble columns, *Can. J. Chem. Eng.* 92 (2014) 1444–1454.
[19] J. Alvaré, M.H. Al-Dahhan, Gas holdup in trayed bubble column reactors, *Ind. Eng. Chem. Res.* 45 (2006) 3320–3326.
[20] K. Mohanty, D. Das, M.N. Biswas, Hydrodynamics of a novel multi-stage external loop airlift reactor, *Chem. Eng. Sci.* 61 (2006) 4617–4624.
[21] K. Mohanty, D. Das, M.N. Biswas, Mass transfer characteristics of a novel multi-stage external loop airlift reactor, *Chem. Eng. J.* 133 (2007) 257–264.
[22] S.M. Teli, C. Mathpati, Hydrodynamic studies in sectionalised external loop air lift reactors, *Indian Chem. Eng.* (2019) 1–16.
[23] M. Atenas, M. Clark, V. Lazarova, Holdup and liquid circulation velocity in a rectangular air-lift bioreactor, *Ind. Eng. Chem. Res.* 38 (1999) 944–949.
[24] V. Sivasubramanian, B. Naveen Prasad, Effects of superficial gas velocity and fluid property on the hydrodynamic performance of an airlift column with alcohol solution, *Int. J. Eng. Sci. Technol.* 1 (2011) 245–253.
[25] M. Utiger, F. Stuber, A.M. Duquenne, H. Delmas, C. Guy, Local measurements for the study of external loop airlift hydrodynamics, *Can. J. Chem. Eng.* 77 (1999) 375–382.
[26] M. Asari, F. Hormozi, Experimental determination of bubble size in solution of surfactants of the bubble column, *J. Adv. Chem. Eng.* 04 (2014) 1–5.
[27] C.P. Ribeiro, P.L.C. Lage, Experimental study on bubble size distributions in a direct-contact evaporator, *Brazilian J. Chem. Eng.* 21 (2004) 69–81.
[28] G. Besagni, F. Inzoli, The effect of liquid phase properties on bubble column fluid dynamics: Gas holdup, flow regime transition, bubble size distributions and shapes, interfacial areas and foaming phenomena, *Chem. Eng. Sci.* 170 (2017) 270–296.
[29] G.R. Guédon, G. Besagni, F. Inzoli, Prediction of gas–liquid flow in an annular gap bubble column using a bi-dispersed Eulerian model, *Chem. Eng. Sci.* 161 (2017) 138–150.
[30] K. Ekambara, M.T. Dhotre, J.B. Joshi, CFD simulations of bubble column reactors: 1D, 2D and 3D approach, *Chem. Eng. Sci.* 60 (2005) 6733–6746.
[31] W.M. Clift, R. Grace, J.R. Bubbles, Drops and Particles, Courier Corporation, 2005.
[32] M. Pourtousi, P. Ganesan, J.N. Sahu, Effect of bubble diameter size on prediction of flow pattern in Euler-Euler simulation of homogeneous bubble column regime, *Meas. J. Int. Meas. Confed.* 76 (2015) 255–270.
[33] S.B.D. Pfleger, Modelling and simulation of the dynamic flow behaviour in a rectangular bubble column, *Chem. Enginnering Sci.* 56 (2001) 1737–1747.
[34] A.A. Kulkarni, J.B. Joshi, Lift force on bubbles in a bubble column reactor: Experimental analysis, *Chem. Eng. Sci.* 63 (2005) 5873–5931.
[35] A. Tomiyama, G.P. Celata, S. Hosokawa, S. Yoshida, Terminal velocity of single bubbles in surface tension force dominant regime, *Int. J. Multiph. Flow.* 28 (2002) 1497–1519.
[36] S. Schwarz, T. Kempe, J. Fröhlich, An immersed boundary method for the simulation of bubbles with varying shape, *J. Comput. Phys.* 315 (2016) 124–149.
[37] D.A. Drew, R.T. Lahey Jr. The virtual mass and lift force on a sphere in rotating and straining inviscid flow, *Int. J. Multi. Flow*. 13 (1987) 113–121.
[38] L.M. Milne-Thomson, Theoretical hydrodynamics, *Bull. Am. Math. Soc.* 47(5) (1941) 352–353
[39] R. Higbie, The rate of exposure ofa pure gas into a still liquid during short periods of exposure, *Trans. Am. Inst. Chern. Eng.* 31 (1935) 365–389.
[40] P.V. Danckwerts, Significance of liquid-film coefficients in gas absorption, *Indus Eng. Chem.* 43 (1951) 1460–1467.
[41] S.S. Alves, C.I. Maia, J.M.T. Vasconcelos, A.J. Serralheiro, Bubble size in aerated stirred tanks, *Chem. Eng. J.* 89 (2002) 109–117.
[42] N. Frossling, Uber die Verdunstung fallenden Tropfen, *Gerlands Beitage Geophysics* 52 (1938) 170–216.
[43] S.S. Joshi, V.V. Ranade, S.D. Gharat, S.S. Lele, Sparged loop reactors, *Can. J. Chem. Eng.* 68 (1990) 705–741.